Title
A lymphocyte chemoaffinity axis for lung, non-intestinal mucosae and CNS

Journal
Nature, 635(8039)

ISSN
0028-0836

Authors
Ocón, Borja
Xiang, Menglan
Bi, Yuhan
et al.

Publication Date
2024-11-21

DOI
10.1038/s41586-024-08043-2

Peer reviewed

nature

https://doi.org/10.1038/s41586-024-08043-2

Accelerated Article Preview

A lymphocyte chemoaffinity axis for lung, non-intestinal mucosae and CNS

Received: 12 March 2024

Accepted: 12 September 2024

Accelerated Article Preview

Cite this article as: Ocón, B. et al. A lymphocyte chemoaffinity axis for lung, non-intestinal mucosae and CNS. *Nature* https://doi.org/10.1038/s41586-024-08043-2 (2024)

Borja Ocón, Menglan Xiang, Yuhan Bi, Serena Tan, Kevin Brulois, Aiman Ayesha, Manali Kunte, Catherine Zhou, Melissa LaJevic, Nicole Lazarus, Francesca Mengoni, Tanya Sharma, Stephen Montgomery, Jody E. Hooper, Mian Huang, Tracy Handel, John R. D. Dawson, Irina Kufareva, Brian A. Zabel, Junliang Pan & Eugene C. Butcher

A lymphocyte chemoaffinity axis for lung, non-intestinal mucosae and CNS

Borja Ocón[#1,2,3*], Menglan Xiang[#1,3*], Yuhan Bi[#1,3*], Serena Tan[1], Kevin Brulois[1,2,3], Aiman Ayesha[1,3], Manali Kunte[2,3], Catherine Zhou[2,3], Melissa LaJevic[2,3], Nicole Lazarus[2,3], Francesca Mengoni[1,5,6], Tanya Sharma[1,3], Stephen Montgomery[1], Jody E. Hooper[1], Mian Huang[4], Tracy Handel[4], John R. D. Dawson[4], Irina Kufareva[4], Brian A. Zabel[2,3], Junliang Pan[#2,3] & Eugene C. Butcher[1,2,3]

[1] Department of Pathology, Stanford University School of Medicine, Stanford, CA, USA. [2] Palo Alto Veterans Institute for Research, Palo Alto, CA, USA. [3] Veterans Affairs Palo Alto Health Care System, Palo Alto, CA, USA. [4]Skaggs School of Pharmacy and Pharmaceutical Sciences, University of California San Diego, 9255 Pharmacy Lane, MC 0657, La Jolla, CA 92093, USA. [5] Department of Neurosciences, Biomedicine and Movement Sciences, University of Verona, Italy. [6] Department of Engineering for Innovation Medicine, University of Verona, Italy.

[#]These authors contributed equally: Borja Ocon, Menglan Xiang, Yuhan Bi, Junliang Pan.

*Correspondence. Email: boconmor@stanford.edu, mxiang1@stanford.edu, yub10@stanford.edu.

Abstract

Tissue-selective chemoattractants direct lymphocytes to epithelial surfaces to establish local immune environments, regulate immune responses to food antigens and commensal organisms, and protect from pathogens. Homeostatic chemoattractants for small intestines, colon, and skin are known[1 2], but chemotropic mechanisms selective for respiratory tract and other non-intestinal mucosal tissues (NIMT) remain poorly understood. Here we leveraged diverse omics datasets to identify GPR25 as a lymphocyte receptor for CXCL17, a chemoattractant cytokine whose expression by epithelial cells of airways, upper gastrointestinal and squamous mucosae unifies the NIMT and distinguishes them from intestinal mucosae. Single-cell transcriptomic analyses show that *GPR25* is induced on innate lymphocytes prior to emigration to the periphery, and is imprinted in secondary lymphoid tissues on activated B and T cells responding to immune challenge. *GPR25* characterizes B and T tissue resident memory and regulatory T lymphocytes in NIMT and lungs in humans and mediates lymphocyte homing to barrier epithelia of the airways, oral cavity, stomach, biliary and genitourinary tracts in mouse models. *GPR25* is also expressed by T cells in cerebrospinal fluid and *CXCL17* by neurons, suggesting a role in CNS immune regulation. We reveal widespread imprinting of *GPR25* on regulatory T cells, suggesting a mechanistic link to population genetic evidence that *GPR25* is protective in autoimmunity[3,4]. Our results define a GPR25-CXCL17 chemoaffinity axis with the potential to integrate immunity and tolerance at non-intestinal mucosae and the CNS.

Introduction

Lymphocyte trafficking is essential to the establishment, organization and function of the immune system. Innate lymphocytes are primed in the thymus to migrate to frontline barriers in mucosal tissues and skin. Naive conventional T and B cells are pre-programmed to home to secondary lymphoid organs where they are activated in response to antigens arriving through afferent lymphatics. During activation they are "imprinted" by environmental factors (presented by stromal cells and migratory dendritic cells) to migrate to target tissues where they carry out effector, regulatory and surveillance functions. Adhesion receptors for vascular addressins provide regional (e.g. GI tract vs skin) specificity, but constitutively expressed "homeostatic" chemoattractant cytokines ("chemokines") expressed by epithelial cells are pivotal in regulating lymphocyte homing and establishing distinct lymphocyte compartments in various barrier tissues. Secreted chemokines bind glycosaminoglycans and are presented by stromal elements and by venous endothelial cells, providing "chemoaffinity" cues for tissue-specific endothelial recognition by blood-borne lymphocytes and haptotactic migration within tissues. Barrier-defining chemokine/receptor pairs have been identified that recruit lymphocytes selectively to the small intestine (CCL25/CCR9), colon (GPR15LG/GPR15), and skin (e.g.

CCL27/CCR10)[1,2,5]. Lymphocyte trafficking also disseminates immune responses to distant sites: Intranasal vaccination provides protective immunity in the vagina and cervix[6,7], a process that involves migration of antigen-specific T cells via the blood to the genitourinary mucosa where subsets establish long term resident memory[8,9]. Intestinal exposure to food antigens and intestinal flora induces regulatory T cells (Tregs) that provide systemic immune tolerance[10], preventing allergic reactions to pulmonary exposure and suppressing inflammatory responses to cross-reactive autoantigens in the CNS[11]. The mechanisms for dissemination of immune responses and cross-talk between organs remain unclear. Moreover, mechanisms of lymphocyte localization to some of the most clinically significant organs in the body including the respiratory tract, upper GI and genitourinary systems have remained poorly understood.

The mammalian lung features terminal alveoli, creating a vast surface area for air exchange but also for exposure to pathogens and allergens. The respiratory tract is uniquely susceptible to airborne agents, but is also exposed to food antigens and oral microbiota inhaled during mouth breathing, as well as intestinal microbes delivered by hand-to-mouth or -nose transmission or contamination. The respiratory immune system must maintain a strict balance between tolerance and inflammation in the face of this broad challenge with antigens and organisms. Given the critical importance of pulmonary homeostasis to survival, we reasoned that evolutionary pressures may have favored development of a homeostatic lymphocyte chemoattractant program for the respiratory tract. Here we harnessed the wealth of data generated by the genomic and single-cell transcriptomic revolutions to identify a homeostatic respiratory chemoattractant receptor and its ligand and elucidate their function. The results provide a comprehensive picture of a chemoaffinity mechanism shared by the airways, non-intestinal mucosa and the CNS, and suggest a prominent role for the pathway in dissemination of regulatory and tissue resident lymphocytes for systemic immunity and immune homeostasis.

Results

GPR25 marks lymphocytes in lung and NIMT

Leukocyte chemoattractant receptors are class A G protein-coupled receptors (GPCRs); thus we initially asked if lymphocytes in the airways can be differentiated from intestinal lymphocytes on the basis of their GPCR expression profiles. Using single-cell transcriptomic data from patient samples derived from the respiratory tract, colon, caecum, and small intestines, we evaluated the expression of 510 class A GPCRs. Scatterplots of mean mRNA expression highlighted selective expression of the orphan receptor *GPR25* in airways (combined nasal cavity, trachea, bronchus samples) compared to both intestinal compartments, while *CCR9* was prominently expressed in the small intestines and *GPR15* in the colon (Fig. 1A; Supplementary Table 1). Differences in airway vs gut T cell expression were consistent across patient samples, and particularly prominent for CD8 T cells (Extended Data Fig. 1A).

GPR25 is a poorly studied GPCR of unknown function. It has been implicated in autoimmunity through genome-wide association (GWAS) and expression quantitative trait locus (eQTL) studies[3,4]. A compendium of cell type and tissue gene expression data indicate that *GPR25* expression is largely restricted to lymphocytes and NK cells, suggesting a unique role for the receptor in lymphocyte biology (Extended Data Fig. 1B and C; Supplementary Table 1). Violin plots reveal that CD4 and CD8 effector/memory cells (TEM), Tregs, and CD8 T resident memory cells (CD8 TRM, identified as *ITGAE* high) in lungs and airways express *GPR25* but not the chemoattractant receptors for colon (*GPR15*), small intestines (*CCR9*) or skin (*CCR10*) (Fig. 1B; Supplementary Table 1). Conversely, *GPR25* is relatively poorly expressed by conventional lymphocytes in the intestines. *GPR25* is also selectively expressed (compared to *CCR9*, *GPR15* and *CCR10*) by T cells in the stomach, pancreas and salivary glands, while *GPR25* and *GPR15* are both expressed by T cells in the genitourinary (GU) tract (data from cervix). In contrast, *CCR9* and *CCR10* are largely restricted to lymphocytes in the small intestines and skin, respectively (Fig. 1B; Supplementary Table 1).

Surprisingly, T cells in cerebral spinal fluid (CSF) of human donors also express *GPR25* (Fig. 1B; Supplementary Table 1). *GPR25* is variably expressed among CSF CD4 and CD8 cells, but is notably high in cells implicated in immune regulation (CD4 Tregs and *FOXP3*+ CD8 cells), and in CD8 TRM (Extended Data Fig. 2). GPR25 may have a role in lymphocyte functions in the CNS, where CD4 cells enhance cognitive development, Tregs control CNS inflammation, and CD8 T cells have both neuroprotective and

neurodegenerative roles[11-13]. Population genetic studies also suggest a potential CNS role: The Brain Catalog database[14] reports Summary-data-based Mendelian Randomization (SMR) for *GPR25* eQTLs for CNS related conditions. SMR leverages genetic variants that affect gene expression as instrumental variables to assess whether gene expression may mediate a disease or trait. Whole blood *GPR25* expression correlated negatively with Multiple Sclerosis (SMR *p*-value=1.5e-9), Schizophrenia (*p*=1.67e-5), Educational Attainment (*p*=2.2e-5) and Cognitive Performance (*p*=1.06e-4).

Among B cells, *GPR25* is highly expressed by barrier tissue-homing *FCRL4*+ B cells in the respiratory tract and lung, and by circulating plasma cells (Fig. 1C; Supplementary Table 1). Innate lymphocyte subsets including γδT cells, NK cells, NK T cells, mucosae-associated invariant T cells (MAIT), innate lymphoid cells (ILC) in the fetal lung, and ILC progenitors (ILCP) in the fetal SI express *GPR25*, while the gene is less well expressed by innate populations in adult lung as a whole, and in intestines (Fig. 1D; Supplementary Table 1). Myeloid cells from blood and tissues evaluated lacked *GPR25* (Extended Data Fig. 1B and C; Supplementary Table 1).

GPR25 regulation and imprinting

Homeostatic chemoattractant receptors display characteristic patterns of regulation reflecting their dual role in seeding mucosal surfaces with innate lymphocytes and targeting the migration of antigen-activated T and B cells. To elucidate the regulation of *GPR25* during T cell development, we evaluated gene expression profiles of human thymocytes (Supplementary Table 1). *GPR25* is upregulated during thymic T cell differentiation in innate populations including NKT, CD8αα unconventional T cell lineages and a subset of TCRγδ cells at a late differentiation stage (colored subsets identified in Fig. 2A), suggesting the potential to contribute to migration of innate T cells to target tissues. Highest expression of *GPR25* defines CD8αα(II) cells, a population that has a mixture of TCRαβ and TCRγδ T cell signatures[15] and comprises thymic precursors of mucosa-homing CD8αα unconventional intraepithelial lymphocytes (IEL)[16].

To assess regulation during lymphocyte activation and differentiation in an immunologically active peripheral lymphoid organ, we evaluated T cells in the human tonsil. The tonsil processes antigens in the oral pharynx contiguous with the trachea and airways. To focus on immunologically responding CD4 T cells, we enriched for T cells expressing activation antigens by fluorescence activated cell sorting (FACS) prior to cell capture for scRNAseq (5' 10x Genomics) (see Methods). A UMAP projection of tSpace (pseudotime) trajectories (tUMAP[17]) reconstructed developmental branches from naive T cells to T follicular helper (Tfh) cells, and to Th17 (*IL17A*+ and/or *IL17F*+) and Treg (*FOXP3*+, *IL2RA*+) phenotypes (Fig. 2B). *GPR25* expression emerges during the transition from naive to Treg and Th17 branches, and on dividing T cells, and expression is enhanced in magnitude and frequency as cells mature, presumably in preparation for exit and migration to target tissues. Naive T cells and most Tfh cells lack the receptor gene. The selective expression of *GPR25* by lymphocytes and its induction on innate cells and on antigen-reactive T cells as they mature to tissue migratory phenotypes are consistent with a role in lymphocyte trafficking.

scRNAseq analysis of activated tonsil B cells revealed *GPR25* upregulation in the transition of naive and immature dividing cells to plasma cells and memory B cells (MBC) (Fig. 2C). *GPR25* expression is particularly enriched among the tissue homing *FCRL4*+ B cell subset, a subset identified as tissue resident sentinel B cells within mucosal epithelia[18] (and see Fig. 1C). Thus *GPR25* is imprinted in tonsils during effector differentiation of activated B and T cells.

***GPR25* is induced on Tregs**

Tissue-specific homing receptors are imprinted during lymphocyte activation in lymphoid tissues, conferring targeted migration of antigen-specific T cells[19,20,21,22]. To assess the tissue-specific imprinting of *GPR25*, we examined the transcriptomes of T cells from human thoracic lymph nodes (TLN, lung-draining) and mesenteric lymph nodes (MLN, intestine-draining) (Supplementary Table 1). We compared *GPR25* with the gene for the small intestinal homing receptor *CCR9*, which in mice is selectively imprinted in MLN. As expected, *CCR9* was expressed by T cells in human MLN and nearly absent in TLN (Fig. 2D). In contrast, T cells in both tissues expressed *GPR25* (Fig. 2D-G).

In TLN, CD4 T effector (Teff) and regulatory cells express *GPR25* similarly (Fig. 2E). In contrast, MLN mature Tregs (identified by high expression of *FOXP3* and *IL2RA*; "Treg hi" cells) more prominently express *GPR25* than CD4 Teff (Fig. 2E). On average, ~80% of Treg hi cells in MLN were *GPR25*+ (Fig. 2E) with mean expression greater than that of their Treg hi counterparts in TLN (Fig. 2E and G). Moreover, while cells with high *GPR25* expression in TLN were enriched for Th1, Th17 and Treg, cells with high *GPR25* in MLN were principally enriched for Treg hi cells (Fig. 2F). Almost all *GPR25*+ Treg hi cells in MLN co-expressed *CCR9*, suggesting local induction in response to gut antigens and metabolites (Fig. 2G). Consistent with this, *GPR25*+ Treg hi cells align late along a pseudotime trajectory from naive CD4 cells; and in MLN, *GPR25* expression arises “later” than *CCR9* (Extended Data Fig. 3A). Most *GPR25*+ Tregs and Teff in the small intestinal lamina propria also co-expressed *CCR9* (Extended Data Fig. 3B). Co-expression of *CCR9* likely explains the presence of *GPR25*+ Tregs in the lamina propria, since the *GPR25* ligand (identified below) is poorly expressed in the normal intestines. Together, these data show that *GPR25* is imprinted on T cells in gut as well as lung-draining lymphoid tissues. Imprinting of GPR25 on Tregs in gut-associated lymphoid tissues may position Tregs to contribute to the systemic dissemination of tolerance to gut microbes and food antigens.

Identification of a GPR25 ligand

We considered potential characteristics of a ligand for GPR25 based on structural features of the receptor. GPR25 is well conserved in vertebrate evolution and contains a canonical DRYLAVV motif in the third transmembrane sequence (Fig. 3A). It has a conserved negatively charged N-terminal extracellular peptide comprising a DY candidate sulfation site characteristic of many leukocyte chemoattractant receptors for positively charged polypeptides of the chemokine family. The closest relative of GPR25 is the colon homing receptor GPR15[23]. CoINPocket analysis[24] indicates that the ligand binding pocket of GPR25 shares similarity to those of GPR15 and bradykinin, apelin, and chemerin receptors that, like GPR15, are activated by C-terminal peptides of their cognate ligands (Fig. 3B). Based on these features we postulated that a physiologic attractant for GPR25 would be a chemokine-like protein (molecular weight < 25 kD) with a net positive charge (pI > 8, facilitating charge-based receptor and GAG binding), and that it would comprise an evolutionarily conserved C-terminal peptide for receptor insertion and activation. We identified 455 genes encoding known or predicted secreted peptides within the expected pI and MW range (Fig. 3C, Supplementary Table 2). Of these, 142 had homologs in multiple species and displayed well conserved C-terminal peptide sequences (Fig. 3D, Supplementary Table 3; alignment of C-terminus of orphan chemokine CXCL17 is shown). To further enrich likely candidates, we assessed patterns of tissue expression: As *GPR25* expression is limited to lymphocytes, we reasoned that expression of a physiologic ligand within tissues might correlate with infiltration of *GPR25*+ cells and thus with *GPR25* message. We evaluated the correlation of *GPR25* with genes for ligand candidates across 49 non-lymphoid tissues with bulk RNAseq gene profiles from the Human Protein Atlas (Supplementary Tables 1 and 4). Tissue expression profiles of *GPR25* and *CXCL17* are illustrated (Fig. 3E).

These criteria converged to identify the orphan chemokine CXCL17 as a candidate GPR25 ligand. The full length CXCL17 protein comprises 6 cysteines but may be cleaved *in vivo* to release a C-terminal peptide with 4 cysteines ("4CysCXCL17") and a predicted MW of 6.6 kD[25]. The peptide displays anti-microbial activity at micromolar concentrations[26] and is implicated in angiogenesis and tumor progression[27]. It has been reported to attract myeloid cells but not bulk lymphocyte populations[28,29,30,31], although published data are inconsistent and the chemotactic potency of CXCL17 for myeloid cells has been questioned[30]. A report that GPR35 is a receptor for CXCL17 is now considered incorrect[32,33,30]. CXCL17 activates the promiscuous mast cell receptor MRGPRX2[34] and can modulate CXCR4 activity on cells via glycosaminoglycan (GAG) binding[35]. CXCL17 does not assume a classical chemokine conformation[30] and evolved independently of the classical chemokine family[23]: it is first found in the genome after divergence of the mammals from other tetropods, and may have emerged in response to the immune challenges associated with evolution of the mammalian lung. It has a predicted MW of ~14 kD and a pI of ~11, and a highly conserved C terminus. Consistent with our hypothesis, *in silico* modeling predicts insertion of the conserved C-terminal FALPL peptide of CXCL17 into the GPR25 signaling pocket (Fig. 3F and Extended Data Fig. 4). A human Ig Fc-h4CysCXCL17 chimeric fusion protein "tracer" binds to cells expressing GPR25, and binding is inhibited by free native h4CysCXCL17 (Fig. 3G).

GPR25 mediates chemotaxis to CXCL17

To determine if GPR25 is activated by CXCL17 and to evaluate its chemotactic function, we established stable L1.2 lymphoid cell transfectants expressing *hGPR25* alone (L1.2^{GPR25}) or with a serum response factor response element (SRF-RE) luciferase reporter (L1.2 $^{hGPR25\text{-}SRF\text{-}RE}$). The reporter quantifies activation of the small GTPase RhoA pathway which regulates cytoskeletal dynamics and integrins during leukocyte chemotaxis[36]. CXCL17 dose-dependently activated L1.2$^{hGPR25\text{-}SRF\text{-}RE}$ cells with an EC50 of ~ 60 nM. A peptide comprising the C-terminal 26 amino acids of mouse CXCL17 (with Cys to Asn substitutions to avoid crosslinking) retained signaling activity, albeit with reduced potency (EC50 ~ 220 nM), whereas truncation of the four C-terminal amino acids "ALPL" rendered the chemoattractant inactive. CXCL17 variants used here are illustrated in Supplementary Table 5. The human GPR15 ligand, GPR15LG, failed to trigger the reporter (Fig. 3H).

L1.2^{GPR25} cells migrated efficiently in transwell chemotaxis assays to h6CysCXCL17 and to h4CysCXCL17 (Fig. 3I), less well to the 26 amino acid C-terminal peptide, but not to C-terminally truncated CXCL17 or to GPR15LG. As indicated in Fig. 3B, GPR25 shows similarity in its ligand binding pocket to the paralogous receptors GPR15, BDKRB2, CMKLR1, and APLNR. The ligands for these receptors (GPR15LG, bradykinin, chemerin and apelin, apela) failed to induce L1.2^{GPR25} migration (Fig. 3I). Host L1.2 cells and L1.2 cells transfected with GPR15 or CMKLR1 migrated to their respective cognate ligands, but failed to respond to CXCL17 (Extended Data Fig. 5A and B). GPR25-dependent migration was inhibited by pertussis toxin (PTX), indicating involvement of chemotaxis-associated $G_{\alpha i}$ proteins, and required a CXCL17 gradient as shown by checkerboard assay (Extended Data Fig. 5C and D). Human and mouse GPR25 confer similar migration to human and mouse CXCL17 (Extended Data Fig. 5 E-G). Together these results identify CXCL17 as a conserved and selective chemoattractant ligand for GPR25.

Human PBMC (Fig. 4) and tonsil (Extended Data Fig. 6 B-D) TCR$\alpha\beta$ CD4+ effector and Treg cells migrate to CXCL17 in transwell chemotaxis assays. Blood CD4 effector cells expressing CD161, a marker associated with barrier tissue homing[37], migrated more efficiently than their CD161- counterparts, suggesting a mucosal fate for the cells responding to CXCL17. To ask if *GPR25* expression correlates with T cell chemotaxis to CXCL17, we subjected PBMC T cells to transwell chemotaxis to CXCL17, performed scRNAseq on the input and migrated cells and evaluated migration efficiency of *GPR25*- vs *GPR25*+ subsets. *GPR25*+ Treg and CD4 effector memory lymphocytes migrated better than their *GPR25*- counterparts, with up to 28% of input *GPR25*-high cells migrating to CXCL17 (Fig. 4B).

Consistent with patterns of *GPR25* expression, innate NK and NKT cells and MAIT but not monocytes or dendritic cells migrated to CXCL17 (Fig. 4C and Extended Data Fig. 6). Blood antibody secreting cells (ASC) displayed robust migration to CXCL17, comparable to migration to CCL28, a well established mucosal ASC attractant[38] (Fig. 4D).

Epithelial and neuronal *CXCL17* expression

CXCL17 is expressed by mucosal tissues[25,27,26,28], but a comprehensive picture of cell type expression across organs is missing. Figure 5A presents pseudobulk *CXCL17* expression by cell types annotated under the Human Protein Atlas and illustrates expression by diverse epithelial cell types including respiratory epithelium, epithelial cells of the esophagus, stomach, biliary tract (liver cholangiocytes), prostate, pancreas, salivary glands and squamous mucosae (Supplementary Table 1). Excitatory and inhibitory neurons in the human and mouse brain and spinal cord express *CXCL17*, contrasting with glia (Fig. 5A and Extended Data Fig. 7; Supplementary Table 1). Epithelial cells of the airways have the highest per cell expression of *CXCL17*, followed by lung alveolar type II cells and secretory cells of the stomach and exocrine glands (Fig. 5A). Expression by epithelial subtypes is similar in trachea, bronchial and nasal tissues (Fig. 5B; Supplementary Table 1). In a comparison of airway from COVID-19 patients vs healthy controls, CXCL17 expression was upregulated in subsets of the airway epithelium of patients with severe disease (Extended Data Fig. 8A; Supplementary Table 1). In a mouse model of psoriasis[31], *Cxcl17* is upregulated in epidermis but remains low compared to NIMT. In a mouse model of spinal cord injury, neurons displayed a transient reduction in *Cxcl17* (Extended Data Fig. 7D). CXCL17 can also be induced in activated endothelium[27]. Together these data are consistent with roles for the chemoattractant in immunity and immune homeostasis.

Anti-sense RNA hybridization reveals histologic patterns of *CXCL17* expression by epithelial cells (Fig. 5C). *GPR15LG* expression is shown for comparison. In the stomach *CXCL17* is highly expressed by glandular epithelium, less so by the surface epithelium. Expression in salivary gland and pancreas is limited to exocrine cells and varies dramatically from one glandular cluster to the next. In the duodenum, scattered cells of the Brunner's gland express the chemokine. Squamous mucosae of the oral cavity, esophagus and conjunctivae express *CXCL17* (Fig. 5A and C). Vaginal epithelium also expresses the ligand[39]. Consistent with the scRNAseq data, RNAscope confirms that *CXCL17* is poorly expressed in small and large intestines. In comparison *GPR15LG* is robustly expressed by colonocytes in the colon but poorly by respiratory and digestive gland epithelia (Fig. 5C and Extended Data Fig. 8B; Supplementary Table 1). Interestingly, *GPR15LG* is expressed with *CXCL17* in most squamous mucosae, including sites of squamous metaplasia in the respiratory tract (Fig. 5A and C). These cell-type specific data are consistent with and extend prior bulk RNAseq and immunohistochemical studies of CXCL17[28,26].

As predicted from scRNAseq data (Fig. 5A), RNAscope identifies *CXCL17* in granule neurons of the human cerebellum (Fig. 5C) and immunohistochemistry shows immunoreactivity for CXCL17 in neurons and axonal projections in white matter (Extended Data Fig. 9). Together with expression of *GPR25* by CSF lymphocytes, these results suggest a role for the GPR25-CXCL17 axis in neuroimmune interaction, whether in recruitment, motility and surveillance or other functions. While we do not elucidate these mechanisms and do not exclude a GPR25-independent role for neuronal CXCL17, we note that compared to *Cxcl17*-/- mice, mice with normal CXCL17 expression have reduced latent herpes virus in the dorsal root ganglia after experimental infection[39] and reportedly have reduced susceptibility to experimental allergic encephalomyelitis[40], implicating CXCL17 in neuroprotection. Moreover, as noted above, human population studies reveal inverse correlation of blood *GPR25* expression with multiple sclerosis and traits associated with cognition, suggesting the importance of evaluating functions of the receptor and ligand in the CNS.

GPR25-CXCL17 axis in lymphocyte homing

We used mouse models to test whether GPR25 mediates lymphocyte localization and accumulation in mucosal tissues. We first injected mixed T cells transduced with *Gpr25* or with control vectors (1:1 ratio) into *Rag1*-/- mice and examined tissues 1 or 7 weeks later, and 5 min after i.v. injection of PE-anti-CD45 antibody to label intravascular cells. In these recipients, which lack endogenous T and B cells, adoptively transferred T cells localize and proliferate to occupy empty niches[41]. Compared to vector control transduced cells, *Gpr25*-transduced T cells preferentially populated the GU tract, stomach, and trachea. *Gpr25* transduced cells showed significant enrichment vs control cells in whole lung isolates after 7 weeks but not at 1 week after infusion, potentially reflecting maturation or repositioning within the lung over time (Fig. 6A).

To ask if GPR25 mediates homing from blood into NIMT, we examined *in vivo* localization of *Gpr25*- and co-injected control vector-transduced T cells 10-12 hours after i.v. transfer into WT C57BL/6N and *Cxcl17*-/- recipients (Fig. 6B-F). Recipient mice received anti-CD31 to delineate blood vessels and discriminate intravascular from extravasated cells. In WT recipients, GPR25 enhanced homing to trachea, stomach, tongue, gallbladder and uterine mucosae, but not to the intestines or control peripheral lymph nodes (PLN) or spleen (Fig. 6B, and confocal images, Fig. 6C-D). The ratio of GPR25 transduced to control cells was high for extravasated cells, but was also elevated for cells still within the vasculature bound to endothelium in trachea, stomach, tongue and uterus, suggesting a role for the receptor in endothelial recognition in CXCL17-expressing target sites. Secreted epithelial *CXCL17* may be presented by venous endothelial cells as has been shown for some chemokines[42], although local endothelial expression has not been excluded. The GPR25 advantage disappeared in *Cxcl17*-/- recipients, suggesting CXCL17 is the principal functional ligand for GPR25 in these organs. Insufficient cells localized to the eye, salivary gland, pancreas, bladder, and CNS (spinal cord, cerebellum or choroid plexus) for analysis.

Within the peribronchovascular interstitium of the lungs, many *Gpr25*-transduced cells localized to bronchi (Fig. 6E and F). In contrast, control cells were enriched near veins, suggesting that initial extravasation involves GPR25-independent mechanisms, potentially CCR4[22] or CXCR6[43]. (In models of pulmonary viral immunity, CXCR6 mediates recruitment of virus-specific CD8 TRM but is downregulated as T cells localize to

bronchial epithelium[43] where GPR25 may dominate). *Gpr25*-transduced and control cells were equally represented in alveolar interstitium away from bronchi. *Gpr25*-transduced cells showed no affinity for bronchioles and failed to segregate from control cells in *Cxcl17*-/- recipients.

CXCL17 deficiency also limits endogenous T cell localization: immunohistologic analyses show that CD8 and CD4 intraepithelial cells are reduced in *Cxcl17*-/- vs WT mice in airways, stomach, uterine horns and gall bladder, while the alveolar interstituim and colon were not affected (Fig. 6G).

We conclude that the GPR25-CXCL17 axis mediates lymphocyte recruitment into the respiratory, upper GI, biliary and GU tracts.

Discussion

Our studies identify GPR25 as a lymphocyte chemoattractant receptor for the NIMT/CNS-expressed chemoattractant CXCL17, and show that GPR25 mediates lymphocyte homing to the respiratory, upper GI, biliary and GU tracts. CXCL17, like GPR15LG, shares chemokine-like features and functions yet evolved independently of the classical chemokine family, suggesting it should be renamed. We propose that these chemoattractant cytokines be designated CLCL1 and 2 (for chemokine-like leukocyte chemoattractant ligands) and their receptors CLCRs (chemokine-like leukocyte chemoattractant receptors).

We provide an atlas of *GPR25* regulation in human lymphocyte development and of *GPR25* and *CXCL17* expression in target tissues: Innate lymphocytes upregulate *GPR25* in the thymus before migrating to barrier tissues, and effector and regulatory B and T cells are imprinted with *GPR25* during peripheral immune responses. Our analyses show that *GPR25* characterizes resident CD8 T cells and FCRL4+ B cells, populations that serve as immune sentinels and modulators in barrier mucosae[44,45]. CXCL17 is most highly expressed in the airways, suggesting the respiratory tract may serve as a central hub for a GPR25-CXCL17 defined immune network. The data also suggest a prominent role for GPR25 in regulatory T cell dissemination. CD4+ Tregs in each of the CXCL17-expressing tissues including the CNS express *GPR25*. More surprising is the imprinting of *GPR25* on gut associated regulatory T cells, cells thought to play an important role in oral tolerance and prevention of autoimmune responses to commensal organisms. GPR25-dependent Treg tropism to the respiratory system, NIMT and CNS may suppress systemic immune responses to benign food and gut microbes; while effector cell migration may contribute to systemic immune surveillance. Indeed, in a study of acute and recurring herpes infection, Srivastava[39] showed that *Cxcl17*-/- mice recruit fewer CD8 TRM and Teff cells to the vaginal mucosa and have reduced protection of the mucosa and of dorsal root ganglia against viral replication and latency. These results are consistent with involvement of the GPR25-CXCL17 axis in protective anti-viral responses at mucosal and neuronal sites. Additional animal models will be required to fully elucidate the protective and pathogenic roles of this pathway in infectious diseases, cancer and autoimmune pathologies, and to understand its interplay with other chemoattractant programs[46] that can contribute to lymphocyte recruitment to mucosal tissues, including lungs and NIMT.

Discovery of the NIMT/CNS chemoaffinity program presents opportunities to understand unexplained aspects of immune system integration and dysregulation in disease. GPR25 induction and directed migration of T cells may explain the effectiveness of intranasal vaccination in protecting the genitourinary tract. As discussed, GPR25 -dependent dissemination of Tregs may help prevent autoimmunity to self-antigens recognized through “molecular mimicry” by T cells responding to intestinal microbes and food antigens. Poor regulatory T cell dissemination could explain the association observed between reduced *GPR25* expression and susceptibility to autoimmune diseases including MS, uveitis, ankylosing spondylitis, primary biliary cholangitis, celiac and inflammatory bowel diseases[3,4,47]. Recent studies in rat models of EAE suggest that pathogenic T cells undergo “licensing”[48] in the respiratory tract before migrating to the CNS to induce disease: GPR25 could mediate lung localization for licensing, and/or migration to or within the CNS. GPR25-dependent recruitment of regulatory or effector T cells could contribute to proposed pro- and anti-tumor effects of CXCL17 in cancers[29]. Future studies must address these possibilities through preclinical and clinical investigation. Our studies also suggest opportunities for disease monitoring and therapy: Antibodies to GPR25 may allow monitoring of vaccine responses and identification of cells involved in pulmonary or NIMT tolerance or inflammation in disease settings. Engineered expression of GPR25 may enhance adoptive regulatory T cell therapies for autoimmune diseases. Thus GPR25 and its ligand define a core axis of the integrated mucosal immune system with broad implications for understanding and manipulating immunity and inflammation. Our

data represent a valuable resource for future investigations into the biology of respiratory/NIMT/CNS lymphocyte traffic and its role in systemic immunity and immune pathogenesis.

Acknowledgements: Funded by NIH grants R01 AI178113 and R01 AI047822, MERIT award I01 BX-002919 from the United States Department of Veterans Affairs Biomedical Laboratory R&D Service (VA BLR&D), Grant 1903-03787 from The Leona M. & Harry B. Helmsley Charitable Trust, and the Regents of the University of California Tobacco Related Disease Research Program (TRDRP) grants T31IP1880 and T33IR6609 to E.C.B.; R21 AI149369, R21 AI156662 to I.K.; R01 AI161880, R01 GM136202 to I.K. and T.M.H.; and R01 MH125244 to S.M. B.A.Z. was supported by Merit Review Award Number I01 BX004115 from the VA BLR&D and by TRDRP grants T32IP5349 and T33IP6514. A.A. was supported by the California Institute for Regenerative Medicine (CIRM), award EDUC2-12677. F.M. was supported by the Department of Excellence 2023-2028 DNBM, the Cariverona Foundation – Research and Development Grant 2022 and the #NEXTGENERATIONEU and the Italian Ministry of University and Research, National Recovery and Resilience Plan (PNRR), project MNESYS (PE0000006). M.X. was supported by the TRDRP grant T31FT1867. Y.B. and B.O. were Research Fellows Awardees of the Crohn's and Colitis Foundation of America (835171 and 574148), and B.O. was a postdoctoral fellow of the Ramon Areces Foundation (Madrid, Spain). We thank Dr Yi Yao for statistics, Dr Baohui Xu for technical advice, Griselda Ramos for mouse colony maintenance and Lourdes Magalhaes for administrative support. Schematic of GPR25 created with BioRender.com.

Author contributions:
B.O., Y.B., A.A., M.K., M.H., J.P., M.X., K.B., M.L., N.L. and F.M. performed experiments. M.X. and K.B. performed single-cell RNA-seq analysis. M.X., C.Z., J.R.D.D., I.K. and J.P. performed in silico analysis and protein modeling. S.T. performed RNAscope. S.M., T.S. performed population genetic analyses. J.E.H. collected autopsy samples. M.H. and T.H. provided reagents. E.C.B., M.X., B.O. and Y.B. wrote, and T.H., B.A.Z., and K.B. edited the manuscript. E.C.B. and J.P. conceived and E.C.B. supervised the study.

Competing interests
The authors declare no competing financial or non-financial interests.

Data availability
Raw and processed single-cell RNA-seq data generated in this study are available from the NCBI Gene Expression Omnibus repository under the accession number GSE273397. Supplementary Table 1 lists all published external datasets used in this study. Integrated scRNAseq datasets used for the analyses can be accessed at http://med.stanford.edu/butcherlab/data/GPR25.html. Source data are provided with this paper.

Code availability
Code for computational analyses is available upon request.

Main figure legends

Figure 1. Human *GPR25* is expressed by lymphocytes in lungs, non-intestinal mucosae and CNS.
A. Expression of *GPR25*, *GPR15* and *CCR9* (black, labeled) and other class A GPCRs (gray) in total CD4/CD8 T cells from airway (combined nasal cavity, trachea, bronchus samples) vs colon (left), and in airway vs small intestine (SI) (right).
B. Violin plots of *GPR25*, *GPR15*, *CCR9* and *CCR10* in CD4 T cell subsets in indicated target tissues. For cells from lungs, presumptive parenchymal vs bronchiolar cells are identified by expression of genes *ITGAL* and *ITGB2* that encode the distinguishing marker LFA-1[43].
C-D. Violin plots of *GPR25* in B cell (C) and T innate (D) subsets in indicated target tissues.
Data shown are pooled from adult and pediatric donors unless specified otherwise. Mean imputed expression values from individual donors (open circles) and mean ± SEM of of the donor means (solid circles) are shown (n=1-33, B-D). Subsets with fewer than 10 cells are not plotted. All samples from healthy donors except: patients with primary Sjogren's syndrome (salivary gland), combined normal and pancreatic ductal adenocarcinoma (pancreas), normal and cognitively impaired (CSF), and HSV-2 seropositive (cervix). Detailed source and meta data in Supplementary Table 1.

Figure 2. *GPR25* induction on innate T cells in the thymus and regulatory and effector T and B cells during peripheral immune activation in human.
A. *GPR25* expression by maturing innate T cells in human thymus. Left: UMAPs of postnatal thymocytes, colored by subset and *GPR25* expression. Immature CD4+CD8+ thymocytes in gray. Data from 3 healthy donors aged 3, 10, and 30 months. Right: violins showing prominent expression by NKT cells and CD8aa(II) mucosal IEL precursors. Means of individual donors (open circles) and mean of means (solid circles) ± SEM. Subset annotation and UMAP from original publication[15].
B. tUMAPs of activated tonsil CD4 T cells showing *GPR25* expression on differentiating CD4 cells. Cells with *GPR25* expression < 0.1 in gray.
C. tUMAPs of tonsil B cells illustrating *GPR25* expression by plasmablasts (PB) and *FCRL4*+ tissue homing B memory cells (MBC). GC, germinal center cells. Cells with *GPR25* expression < 0.05 in gray.
D-G. Expression of *GPR25* and *CCR9* by T cells from lung-draining thoracic LN (TLN) and SI-draining mesenteric LN (MLN), pooled from 14 MLN and 9 TLN healthy donors.
D. UMAP illustrating *GPR25*+*CCR9*-, *GPR25*-*CCR9*+ and *GPR25*+*CCR9*+ T cells. *GPR25*+ and *CCR9*+ defined by expression > 0.1.
E. Mean *GPR25* expression and percent *GPR25*+ cells within T cell subsets from individual MLN and TLN donors (open circles), presented with mean of donor means (solid circles) ± SEM. Solid lines: comparison between different subsets within MLN (black) or TLN (red). Dashed lines: comparison of the same subset between different tissues. ***: *p*-value < 0.001; n.s.: non-significant, multivariate regression.
F. Representation of subsets among MLN and TLN T cells expressing different levels of *GPR25*.
G. Dot plots of mean *GPR25* vs *CCR9* expression by T subsets from independent MLN and TLN donors, illustrating co-expression of *CCR9* and *GPR25* by Tregs and Teff in the MLN. Ellipses are 1 standard deviation around mean of the replicate sample means. **A-G**. All gene expression imputed.

Figure 3. Bioinformatic discovery of a GPR25-CXCL17 lymphocyte chemoattractant axis.
A. Schematic of GPR25 protein structure.
B. Similarity of ligand binding pocket of GPR25 to that of other Class A GPCRs.
C. Isoelectric point (pI) and molecular weight (MW) of human secreted proteins. Chemokines (black) and ligands of interest are highlighted. Square indicates predicted pI > 8 and MW < 25kD.
D. C-terminal conservation of proteins gated in C. Upper panel: mean BLAST bit-scores calculated from pairwise alignment of C-terminal 6 amino acids of the human protein and orthologs in mouse, rat, rabbit, dog, and cow. Square indicates BLAST score > 4. Lower panel: C-termini of CXCL17 in indicated species. Red indicates mismatch with human.
E. *GPR25* correlation with candidate ligands gated in D across 49 tissues assessed by bulk RNAseq. Scaled log-transformed tissue profiles of *GPR25* and *CXCL17* shown in lower panel.
F. AlphaFold model of human (h)4CysCXCL17 (red) interaction with GPR25 (blue), illustrating insertion of C-terminal FALPL peptide of CXCL17.
G. Human IgFc-4CysCXCL17 chimera ("tracer") binding to GPR25-expressing vs control CHO cells, and

inhibition by unlabeled native 4CysCXCL17. Representative of four experiments. N=3 per condition.
H. CXCL17 activation of RhoA signaling pathway through GPR25. Serum response factor response element (SRF-RE)-driven luciferase reporter activity of GPR25-transfected L1.2 cells incubated with the indicated amounts of human (h)4CysCXCL17, mouse CXCL17 26aa C-terminal peptide (mCXCL17 26aa C-term), human 4CysCXCL17 C-term-truncated and human GPR15LG. Sequences of CXCL17 variants are in Supplementary Table 5. One experiment representative of three. Mean of 2 replicates per condition.
I. Transwell chemotaxis of human GPR25-transfected L1.2 cells to indicated chemoattractants or ligands illustrating selective migration to CXCL17 variants with intact C terminus. NC: no chemokine control. N = 3-6 per condition. Pooled from 2 or more experiments. In G and I, data shown as mean ± SEM.

Figure 4. Chemotaxis of blood lymphocytes to CXCL17.
A-D. Transwell migration of blood T cells (A, B), innate lymphocytes and myeloid cells (C) and antibody secreting cells (ASC) (D). PBMC (A, C, D) or purified T cells (B) were migrated to the indicated chemoattractants for 3 hr. Migrated and input subsets were quantified by flow cytometry (A, C), scRNAseq (B) or ELISPOT[38] (D). Data in A and C are % of input cells migrated above mean background in the absence of chemokine (subset-specific background migration indicated in Extended Data Fig. 6A). Data in B and D are % of input T cells subseted by *GPR25* expression (B) or by IgA or IgG secretion (D). Representative gating and sorting strategies summarized in Supplementary Fig. 1A-C. In A, results pooled from four experiments except hGPR15LG and hCCL25 (two), and h4CysCXCL17 30nM, 1μM and 3μM (one). In B, results from one blood donor but representative of two. In C and D, results pooled from three experiments except for hGPR15LG and CCL25 (one). Data shown as mean (B) or mean ± SEM (A,C and D) with an n = 3-15. * P<0.05, ** p<0.01, *** p<0.001, **** p<0.0001. One way ANOVA with Dunnet post hoc tests comparing the indicated condition vs no chemokine controls (NC).

Figure 5. Subset- and tissue-selective epithelial and neuronal expression of *CXCL17*.
A. Pseudo-bulk expression of *CXCL17* by epithelial cell subsets and other cells from various tissues (Human Protein Atlas). Data represent normalized gene expression by subsets of the indicated cell classes and are shown with means of individual samples.
B. Violin plots illustrating imputed expression of *CXCL17*, *GPR15LG* and *CCL25* by airway epithelial cells in healthy donors, presented with means of individual donors (open circles) and mean of donor means (solid circles) ± SEM (n=1-16). Subsets with fewer than 10 cells are not plotted. N, nasal cavity; T, trachea; B, bronchus.
C. Histologic localization of *CXCL17* gene expression: RNAscope was performed using probes for *CXCL17* (blue) and *GPR15LG* (red) in sections of the indicated tissues. Asterisk adjacent to *CXCL17*+ alveolar epithelial cells. Arrows highlight *CXCL17*+ conjunctival epithelium: epithelium overlying the cornea is negative. Neurons are cerebellar granule neurons. Results representative of 3 or more sections from 2-4 donor samples. Scale bars: 100μm, except 25μm for neurons.

Figure 6. CXCL17 and GPR25 in T cell localization to airways, upper GI, biliary and GU tracts.
A. Ratio of GPR25 to control vector-transduced donor cells recovered 1 or 7 weeks after i.v. injection into *Rag1*-/- mice. Normalized to mean of spleen and PLN. Representative gating strategies summarized in Supplementary Fig. 1D. Two (1 wk) or one (7 wk) independent experiments with 7-8 recipients/timepoint. Two 7wk recipients were male. Shown with mean ± SEM. **B.** Ratio of GPR25 to control transduced injected cells, distinguished by fluorescent labels 10-12h after i.v. transfer. Intravascular or extravasated cells assessed by confocal microscopy of whole mounts or sections. Fisher's exact test comparing pooled counts in tissues vs spleen in WT recipients (+ P<0.001); or comparing *Cxcl17*-/- vs WT (* P<0.05). Data from 1 (gallbladder) or 3-4 experiments with one recipient per condition and experiment. Shown with mean. **C-E.** Images of trachea (C), lymph node (D) and section of lung (E) 10-12 hours after injection of ~1:1 GPR25 (green) and control (red) CD4 T cells. **E.** Arrowheads: *GPR25* transductants localized to bronchus (Br). Asterisks: cells near veins (V).
F. Ratio of GPR25 to control cells within 30 μm of bronchial basement membrane (Bronchi); 30 μm of or in contact with venous endothelium (Vein); or within alveolar areas (Alveoli). Each dot is the ratio within a 10x field (~4 mm^2/field). Data from 2-6 fields/mouse from 3 independent experiments, 1 WT and 1 *Cxcl17-/-* mouse per experiment. Mean ± SEM. **G-H.** Immunofluorescence quantification of endogenous T cells in epithelia of indicated organs. Data as cells per cross-sectional area of epithelium from 2-5 sections/mouse, 3-4 mice per group. Mean ± SEM, n ≥ 9. **I.** CD8αβ IEL in WT vs *Cxcl17*-/- mouse bronchiole or stomach. CD103+(*);

CD103- (arrows). Two-tailed T test (A and F) and bivariate linear regression analyses (G-H). *, P < 0.05; **, P < 0.01; ***, P <0.001; ****, P < 0.0001.

Material and Methods

Mice and human subjects

All mice in this study were maintained in specific pathogen-free (SPF) facilities at the Veterans Affairs Palo Alto Health Care System (VAPAHCS). B6/SJL Prprc Pep3BoyJ (CD45.1), C57B6/J CD45.2 and *Rag1-/-* mice were purchased from Jackson laboratories. The *Cxcl17-/-* mouse strain (C57BL/6N*A*^{tm1Brd} *Cxcl17*$^{tm1b(EUCOMM)Wtsi}$/MbpMmucd) RRID:MMRRC_047263-UCD, was obtained from the Mutant Mouse Resource and Research Center (MMRRC) at University of California at Davis, an NIH-funded strain repository, and was donated to the MMRRC by The KOMP Repository, University of California, Davis. Originating from Kent Lloyd, UC Davis Mouse Biology Program mice were purchased from the MMRRC at UC Davis. C57B6/N controls were purchased from the MMRRC as well. Animals were maintained in accordance to US National Institutes of Health guidelines, and experiments were approved by Stanford University Institutional Animal Care and Use Committee. Mice were used at 8-12 weeks of age unless otherwise stated and both sexes were included in experiments, except for homing experiments where the female GU tract was required. Sample size was determined by power analyses based on historical variation in similar studies, or by practical experimental or financial constraints.

Human peripheral mononuclear cells (PBMC) were obtained from healthy donors and surgically removed tonsils were from the Pathology Tissue Bank, Stanford University, Department of Pathology. Some tissues for RNAscope and IHC were collected sterilely from rapid research autopsies by the Research Autopsy Center at Stanford (RACS), consented under Stanford IRB 63818 and autopsy consent. The study was carried out in accordance with the recommendations of the US National Institutes of Health guidelines, with written informed consent from all subjects. The protocol was approved by the Stanford University Institutional Review Board.

Leukocyte isolation from organs and flow cytometry cell phenotyping

Intestinal lamina propria cells were isolated as previously described[49] with minor modifications. To digest the intestines we used the gentleMACS octo dissociator with heaters and C-tubes (Miltenyi). Lung, salivary gland, GU tract, stomach and esophagus were processed and cells isolated as previously described[50]. Brain leukocytes were isolated following a modified version of the following protocol[51]. Following advice from Dr. Gabriela Constantin (University of Verona, Italy), the digestion step after the mechanical dissociation was performed with Liberase TL (Roche) and we applied a percoll gradient-based isolation spinning the cell preparation at 4C to enhance cell viability.

Isolated mouse leukocytes were surface-stained with monoclonal anti-mouse antibodies: BV421 anti mouse Ki67 (16A8), BV650 anti mouse CD69 (H1-2F3), PercpCy5.5 anti mouse TCRγδ (GL3), AF700, anti mouse NK1-1 (S17016D), APCCy7 anti mouse CD3 (145-2c11), BV421 anti mouse CD8β (Ly-3), AF647 anti mouse CD90.1-Thy1.1 (OX-7) and BV711 anti mouse CD4 (RM4-5) were purchased from Biolegend. FITC anti mouse CD45.2 (104), BV605 anti mouse IgA (C10-1), BUV395 anti mouse CD45.1 (A20), BV786 anti mouse CD103 (M290) and BUV737 anti mouse B220 (RA3-6B2) were purchased from BD. PercpCy5.5 anti mouse CD11a (M17/4) and PECy7 anti mouse TCRβ (H57-597) were purchased from Tonbo. PercpCy5.5 anti mouse CD45.1 (A20) was purchased from eBiosciences. AF700 anti mouse CXCR6 (221002) was purchased from R&D.

Isolated human leukocytes were surface-stained with monoclonal anti-human antibodies: PE anti human CD161 (HP-3G10), PE-Cy7 anti human CD103 (Ber-ACT8), PercpCy5.5 anti human CD45RA (HI100), AF700 anti human CD69 (FN50), APC-Cy7 anti human CD25 (M-A251), BV421 and PercpCy5.5 anti human CD3ε (UCHT1), BV785 anti human CD4 (RPA-T4), BV650 anti human CD19 (HIB19), APC anti human CD14 (HCD14), BV605 anti human CD45RO (UCHL1), BV650 anti human CD62L (DREG-56), PE anti human CD123 (S18016C), BV421 anti human HLA/DR (L243) and BV650 anti human CD11c (Bu15) were purchased from Biolegend. BUV395 anti human CD8β (2ST8.5H7), BUV737 anti human TCRαβ (T10B91A-31), BV711

anti human TCR Vα7.2 (OF 5A-12), BUV395 anti human CD56 (NCAM16.2) and FITC anti human CD16 (3G8) were purchased from BD. APC anti human TCRγδ (11F2) was purchased from Miltenyi.

Staining for intracellular Foxp3 was performed using the transcription factor staining kit (eBioscience) and the anti-mouse Foxp3 antibody (150D) from Biolegend or anti-human Foxp3 antibody (PCH101) from eBioscience. Cell viability was always determined using fixable Aqua (510) live / dead cell stain (1:250) (Thermoscientific).

Retroviral transduction for tropism and short-term homing experiments

1 or 7 week long cell tropism experiment

The coding region of mouse GPR25 or a stuffer sequence (empty vector) was cloned into the MSCV-IRES-Thy1.1 retroviral construct (purchased from Vectorbuilder). Retroviruses were generated by transient transfection of Platinum-E (Plate-E) cells as in [52]. Mouse T CD4 naive or total T cells were isolated from the spleen of B6/SJL Prprc Pep3BoyJ CD45.1 and C57B6/J CD45.2 mice (Jackson laboratories) by magnetic negative selection using the Mouse T CD4 isolation kit (STEMCELL technologies). T CD4 cells were stimulated with plate bound 5 μg/ml of anti-mouse CD28 (37.51, eBiosciences) and 10 μg/ml of anti-mouse CD3 (145-2c11, eBiosciences) in RPMI-10. On day 1 and 2 after activation, cells were transduced with retroviruses with the following spinfection conditions (850g, 32C, 4 hours with 8 μg/ml of polybrene). On day 3, the cells were washed and transferred to a different plate under 130 U/ml of mouse IL2 and 10 ng/ml of mouse IL7 (Peprotech). On day 5 cells were harvested and purified with a histopaque 1.077 density gradient. The CD45.1 for mouse GPR25 and CD45.2 for empty vector (and vice versa) transduced cells, were mixed at 1:1 ratio and 20-30 million total cells were injected i.v. into the recipient mice (*Rag1*-/-). 1 week after cell transfer, 2 μg PE-CD45 (30-F11) antibody from Biolegend was injected i.v. in 100μl of PBS 5 minutes before sacrifice to identify and exclude intravascular cells. Cells were then recovered from organs and analyzed by flow cytometry. Only TCRβ+ CD4+ Thy1.1+ cells were considered for analysis and GPR25 / empty vector ratios were calculated for each organ.

Short term competitive homing

Culture and transduction conditions were the same as above. However, here only C57B6/J CD45.2 mice were used as donors and on day 5 of culture only transduced (Thy1.1+) cells were magnetically isolated using CD90.1 microbeads (Miltenyi). Importantly, only transduced cells (>95% purity) were maintained in culture after this point. Mouse GPR25 and empty vector transduced cell cultures were maintained for 2 days under IL2 and IL7 as indicated above. On day 7 mouse GPR25 cells were labeled with CFSE and empty vector cells with Yellow fluorescent dye (Thermoscientific), washed and subsequently mixed at a 1:1 ratio. CFSE and yellow fluorescent dye labeling was performed at 5μM in RPMI with 2% FBS at 37C in a water bath with gentle agitation for 20 minutes. Dyes were switched in one of the 4 independent experiments shown, with comparable results. A total of 20-30 million total cells were injected i.v. into the recipient mice (WT C57B6/N or *Cxcl17*-/-). 10-12 hours later the mice were injected with anti-CD31 (DyLight 633, clone 390, InvivoMab) antibody 30 minutes before sacrifice to identify blood vessels. Subsequently, the mice were sacrificed and organs analyzed by flow cytometry (PLN, spleen) and confocal microscopy (whole mount (trachea, uterine horns) or frozen sections (all the rest)). Results are shown as the ratio of GPR25 transduced to control empty vector transduced cells in either whole organs or specific organ compartments. For analyses of microenvironmental localization in the lungs, the distance of cells to histological landmarks (bronchial basement membranes or veins in the lungs) were measured using the Imaris software.

RPMI-10: RPMI 1640 with L-glutamine, 10% FBS, Pen/Strep, 1X MEM Non-essential amino acids, 1 mM sodium pyruvate, 50 μM b-mercaptoethanol and 1 mM HEPES.

Chemoattractants

Human CCL25, GPR15LG and CXCL12 were purchased from Peprotech. Human chemerin mouse and human 6CysCXCL17 were purchased from R&D. The following peptides were purchased from Phoenix Pharmaceuticals: synthesized human 4CysCXCL17, mCXCL17 26aa C-term, bradykinin, apelin-36 and apelin-32. Human 4CysCXCL17 and human 4CysCXCL17 truncated in the C-terminus (lacking the last 4 amino acids, ALPL) were produced in *E.coli* as follows:

Recombinant h4CysCXCL17 (containing residues 64-119 of human CXCL17) or its C-term truncated mutant (containing residues 64-115) were cloned onto the 3' end of His_8-tagged ubiquitin-3D3 in a pHUI3D3 vector. The plasmids were transformed into One Shot™ BL21(DE3)pLysS Chemically Competent *E. coli* cells (Invitrogen™). Cells were grown to an optical density of 0.6-0.7 in Luria-Bertani medium at 37C, and protein expression was induced by adding 1 mM of isopropyl β-D-1-thiogalactopyranoside. After 6 hours of induction at 37C, cells were harvested by centrifugation, resuspended in lysis buffer (50 mM Tris, pH 7.5, 150 mM NaCl) with addition of benzonase (New England Biolabs), and lysed by sonication. The cell pellet containing CXCL17-4C inclusion body was spun down at 12,000x g, 4C for 15 minutes. The pellet was then solubilized and sonicated in 50 mM Tris, 6 M guanidine-HCl at pH 8, and centrifuged at 12,000x g, 4C for 15 minutes. The resulting supernatant was passed over a gravity column filled by Ni-NTA agarose (Invitrogen™). The resin was washed with 50 mM MES, 6 M guanidine-HCl at pH 6, and protein was eluted with 50 mM sodium acetate, 6 M guanidine-HCl at pH 4. The eluate was adjusted to pH 7 and reduced by 4 mM DTT at room temperature for 2 hours. Then it was diluted 25-fold with refolding buffer (50 mM Tris, 500 mM arginine-HCl, 1 mM EDTA, 1 mM glutathione disulfide, pH 7.5) and slowly stirred at 4 ℃ overnight. The refolded protein was dialyzed in 20 mM Tris, pH 8.0 and 200 mM NaCl. After dialysis, His_8-tagged ubiquitin-3D3 was cleaved by home-made deubiquitylating enzyme Usp2cc for approximately 48 hours[53 54]. The cleaved product was loaded to a reversed-phase Vydac™ 218TP C18 HPLC Column (Grace™) (buffer A: 0.1% trifluoracetic acid; buffer B: 0.1% trifluoroacetic acid; 90% acetonitrile). With linearly increasing buffer B concentration from 33 to 45%, pure h4CysCXCL17 and the C-term truncated mutant were eluted at around 37% and 35% of buffer B, respectively. Formation of two disulfide bonds in each protein was confirmed through conducting intact protein analysis by MALDI-TOF and ESI-TOF mass spectrometry in Center for Metabolomics and Mass Spectrometry, The Scripps Research Institute. The pure proteins were lyophilized and stored at −80 °C until usage.

In vitro chemotaxis assays

L1-2 cells were stably transfected by electroporation with a pcDNA3.1 vector encoding human GPR15, human GPR25 or human CMKLR1 as described[55]. L1-2 transfectants were routinely maintained under G418 500 μg/ml and stimulated with 5 mM butyrate 16 hours before the assay. The L1.2 cell line has been described [56] and used extensively as a host cell for GPCR function studies by us and others. The cells were maintained for suspension growth by serial passage of culture supernatants, and were tested for mycoplasma.

Human PBMCs were isolated from heparinized peripheral blood (10–40 ml) that was obtained *via* venipuncture from healthy donors. Blood samples were processed using ficoll density gradient centrifugation (Histopaque-1077, Sigma-Aldrich). The resulting interface containing the PBMC layer was extracted, washed twice with PBS, and resuspended in RPMI-10. Tonsil cells were mechanically isolated from the surgical specimens and purified with a ficoll density gradient centrifugation as well. Cells were stored frozen in FBS with 10% DMSO until assayed. Frozen PBMC and tonsil cells were incubated for 2 hours at 37C in chemotaxis medium (RPMI-10) to recover. Transwell chemotaxis assays were performed as previously described[2], with the exception of the checkerboard assay where in some wells human 4CysCXCL17 was placed at 250 nM both at the top and bottom chambers of the transwell insert. Cells were migrated for 3 hours, and migrated and input cells analyzed by flow cytometry to assess the percent of input cells that migrated to the bottom well.
Subsets in Figure 4 A and C, as well as Extended Data Figure 6 B-D were immunophenotypically defined as follows: Naive (CD45RO- CD45RA+) or indicated effector/memory (CD45RO+ CD45RA-) TCRαβ+ CD4+ subsets were defined with MAbs to intracellular Foxp3 and CD25 (Tregs), and CD161, a marker of mucosal tissue homing T cells. NK cells were defined as CD14-, HLA/DR-, CD3-, CD19-, CD56+, CD16-. NKT shared the same immunophenotyping but were gated as CD3+. Conventional dendritic cells (DC) were defined as CD3-, CD19-, CD14-, HLA/DR+, CD11c+. Plasmacytoid dendritic cells (pDC) were defined as CD3-, CD19-, CD14-, HLA/DR+, CD123+. Monocytes were defined as CD3- CD19- CD14+, HLA/DR+.
Fortessa (BD) flow cytometer and FlowJo software were used for analyses of input and migrated cells. As indicated in figure legends, the results are presented either as % migration, or as % specific migration. The % specific migration is calculated independently for each subset by subtracting the % migration of the subset in the absence of added chemoattractant (the "no chemokine" control).
Antibody secreting cells[16] were quantified by ELISPOT for IgG and IgA as previously described[38].

Human blood T CD4 cells *in vitro* chemotaxis analyzed by scRNAseq

Blood was collected by venipuncture from healthy donors and PBMC were isolated with a ficoll gradient. T cells were isolated by negative magnetic selection using the total T cell isolation kit (STEMCELL technologies). T cells were then rested for 2 hours in RPMI-10 at 37C and subsequently used as input in a transwell-based chemotaxis assay using h4CysCXCL17 300nM as chemoattractant as described above. Migrated cells were recovered from 9 independent transwell wells and along with the corresponding input samples, separately hashtagged and finally mixed together in preparation for a single 5' 10x Genomics scRNAseq capture. The captured sample was subsequently processed with the 10x genomics v3 kit and sequenced on the Illumina NovaSeq X platform. A total of 3892 input cells and 11367 cells that migrated to h4CysCXCL17 were recovered and analyzed. CD4 Treg and Tem cells were identified as indicated in the "Single-cell RNA-seq data analysis" section below, and % migration of subsets defined by *GPR25* expression levels were determined as for flow cytometry-based assays discussed above.

Human tonsil B and T cell scRNAseq experiment

A human tonsil specimen obtained by surgical resection was mechanically processed and cells were preserved frozen. Cells were later thawed and stained with the following flow cytometry panel: anti human CD45RA-FITC (HI100), anti human HLA -PercpCy5.5 (L243), anti human TCRαβ-BUV737 (IP26) and anti human IgD-BUV395 (IA6-2) antibodies from BD: anti human CD69-PECy7 (FN50), anti human CD45RO-BV605 (UCHL1), anti human CD8-BV421 (SK1), anti human CD4-BV786 (SK3), anti human CD38-APCCy7 (HIT2) and anti human CD19-AF700 (HIB19) antibodies from Biolegend. Cells were FACS sorted as follows using an Aria III sorter (BD) and the indicated number of cells from each subset were combined for 5' 10x genomics scRNAseq capture. Gating strategy shown in supplementary material.
T cell sample: CD45RA+CD45RO+ CD4+ T Cells (20K), HLADR+ CD38+ CD4 T Cells (50K) and total TCRαβ+ CD4+ cells (10K).
B cell sample: TCRαβ- CD4- CD8- non-T cells (20K), TCRαβ- CD4- CD8- IgD- (20K), TCRαβ- CD4- CD8- IgD- CD38+ (20K), TCRαβ- CD4- CD8- IgD- CD38+++ (15K).
The captured samples were processed with the 10x genomics v2 kit and sequenced on the Illumina NovaSeq platform. Data was analyzed as indicated in the "Single-cell RNA-seq data analysis" section below.

Single-cell RNA-seq data analysis

Data integration and processing

Published 5' 10x Genomics scRNAseq data from the human airway[57,58], lung[57,59,60], stomach[61], pancreas[62], salivary gland[63], CSF[64], cervix[65], small intestine[59,66], colon[59,66], skin[67], blood[58,59], thymus[15], and lymph node[59,66] were processed to evaluate leukocyte chemoattractant receptor expression. 5' 10X Genomics scRNAseq data from the Human Protein Atlas[68] was analyzed for cell type-specific *GPR25* expression (GPR25 message is essentially undetectable in 3' scRNAseq data). 3' or 5' 10X data from the human airway[58], gut[59,66], brain[69,70] and other tissues[68], and the mouse brain[71] and spinal cord[72] were assessed for *CXCL17* expression. For data generated in this study, reads were mapped to the GRCh38 reference genome using Cell Ranger. Hashtag demultiplexing was performed using the *HTODemux* function of the "Seurat" package[73,74]. Per cell normalization of raw count data was performed using the *NormalizeData* function of "Seurat" or the deconvolution method implemented in the *computeSumFactors* function from the "scran" package[75]. Count data was log transformed using the *logNormCounts* function from the "scater" package[76] with a pseudo count of 1. The "batchelor" package was used to perform between batch normalization of gene expression using the multiBatchNorm function[77]. When published UMAP coordinates were unavailable, data was integrated using the *fastMNN* function from the "batchelor" package[77] and UMAPs were computed using the R implementation from the umap package[78]. Gene imputation was performed on log-normalized count data within each batch using the original implementation of the MAGIC (Markov Affinity-based Graph Imputation of Cells)[79] algorithm with optimized parameters (t = 2, k = 9, ka = 3). Imputed data was presented in all figures and for trajectory analysis we used magicBatch (https://github.com/kbrulois/magicBatch) followed by tSpace[17].

Cell type identification

Gating for T and B cells was performed using imputed data on the integrated datasets. For T cells, only cells that were *CD45*+, *CD14*- and *CD3E*-high were included for downstream analysis. Innate T cells including NK, NKT, MAIT, $\gamma\delta$T and ILC were defined according to the original published annotation of the respective datasets. CD4 T cells were defined as *CD4*-high, *CD8A*-low and *CD8B*-low. Subsets of CD4 T cells were defined sequentially as follows: regulatory T cells (Tregs) were defined as *FOXP3*+ and *IL2RA*+; T helper 17 cells (Th17) were defined as *FOXP3*- and *IL17A/F*+; CD4 naïve cells were defined as *FOXP3*-, *IL2RA*-, *CCR7*-high, *SELL*-high, and negative for peripherally induced chemoattractant receptors (*CCR1/2/3/4/5/6/8/10*, *CXCR3/5/6* and *CX3CR1*); T follicular helper cells (Tfh) were defined as *FOXP3*-, *IL2RA*-, *TOX*+ and *CXCR5*+; from the remaining cells CD4 central memory cells were defined as *FOXP3*-, *CCR7*-high and *SELL*-high; and Type 1 T helper cells (Th1) were defined as *FOXP3*-, *TBX21*+ and *IFNG*+. CD8 T cells were gated as follows: CD8 naïve cells were defined as *CCR7*-high, *SELL*-high and negative for the chemoattractant receptors as listed above; CD8 central memory cells were defined as *CCR7*-high and *SELL*-high; among the remaining cells tissue resident memory cells were defined as *ITGAE*+; and effector memory cells were defined as *ITGAE*-. For B cells, plasma cells were defined as per the original labels of the respective datasets. Target tissues lack naïve cells, therefore non-plasma cells were defined as B memory cells, among which cells that were *FCRL4*-high were defined as *FCRL4*+ MBC. Tonsil B cell subsets were identified by a combination of Leiden clustering and expression of markers as described[80]. For scRNAseq data of the thymus and tissues analyzed for *CXCL17* expression, as well as the bulk RNA-seq data of the PBMC[81], cell type annotations from the original publications were used.

GPCR binding site similarity analysis

Pairwise GPCR binding site similarity data was obtained from Supplementary Dataset 1 of Ngo *et al* [82].The GPCR-CoINPocket score was used to quantify the similarity between GPCR binding sites based on their contact strength profiles. The pairwise similarity data was compiled into a matrix format, and the GPCR labels were matched to official HGNC gene symbols, with any outdated symbols manually updated. Briefly, GPCR-CoINPocket performs a sequence alignment for the transmembrane domains of all GPCRs analyzed, and using the ligand interaction patterns across all Pocketome entries, the pairwise similarities of GPCR TM domain sequences were calculated and normalized to control for evolutionarily-conserved TM domain regions. The normalized similarity scores were averaged to generate a final binding site similarity score.

Protein analysis for GPR25 ligand search

Isoelectric point (pI) and molecular weight (MW) of human secreted proteins[83] were calculated in R using the "Peptides" package. Proteins with pI > 8 and MW < 25 kD were identified, and amino acid sequences of the human, mouse, rat, rabbit, dog, cow orthologs were obtained from Ensembl BioMart[84]. To evaluate C-terminal conservation of candidate ligands, sequences of the C-terminal 6 amino acids of all proteins were extracted, and the human C-terminal peptide was aligned with that of each of the other 5 species, where ortholog is present, and sequence similarity was calculated by Protein BLAST[85,86]. The BLAST bit-scores from all pairwise alignments were averaged for each protein. To determine correlation of tissue expression profiles between C-terminally conserved candidate ligands and *GPR25*, bulk RNA-seq data for 49 human tissues (excluding lymphoid tissues) were obtained from Human Protein Atlas[87], and Pearson correlation was performed for the cross-tissue gene expression profiles of *GPR25* and the candidate ligands with mean BLAST bit-score > 4.

Cold competitive assay of CXCL17 binding to GPR25

CHO-K1 cells transfected for human GPR25 expression were from DiscoverX, Inc. (Fremont, CA, USA). GPR25 transfectants or normal CHO-K1 cells were incubated in binding buffer [HBSS Ca^{2+}/Mg^{2+} with FBS 2% (v/v)] for 30 min at 4C with 100 nM of either human IgG-Fc or a chimeric protein comprising the human 4CysCXCL17 linked to human Fc through the 4CysCXCL17 N-terminus ("tracer") (Curia Inc., Belmont, CA, USA).

For "cold competition binding assay," GPR25 transfectants were pre-incubated for 30 min with control media or with several concentrations (0.3 nM to 1 μM) of the native h4CysCXCL17 (Phoenix) in binding buffer. Then the "tracer," here human 4CysCXCL17 linked to human Fc, was added to the cells at a concentration of 100 nM and incubated for 30 min.

Finally, the cells were washed in staining buffer (PBS BSA 0.5%), then stained with PE-Goat F(ab')2 anti human IgG (Invitrogen), and acquired on a Fortessa (BD), using FACS Diva Software.

GPCR activation assay

L1.2 hGPR25-SRF-RE stable transfectants were established via electroporation of pcDNA3.1(+)-N-HA-hGPR25 (Genescript) and pGL4.34[luc2P/SRF-RE/Hygro] (Promega), followed by the selection with G418 (500 μg/ml) and Hygromycin B (400 μg/ml). Prior to conducting the assay, cells were stimulated with 5 mM butyrate for 16 hours and subsequently subjected to serum starvation in RPMI medium containing 2% FBS for 2 hours. For the assay, cells were seeded in 12-well plates at 1.5 x 10^5 cells per well and incubated with ligands for 4 hours at 37°C/5% CO2 in RPMI-10. After treatment, cells were harvested and lysed using Lysis Reagent (E1531, Promega). Luminescence was measured using the Promega ONE-Glo EX Luciferase Assay System with reading taken on Turner Biosystems Photometer 20/20n luminometer. Results were normalized by protein concentration.

RNAscope studies

From archival formalin fixed paraffin embedded material, sections were cut at 5 µm. Single molecule in situ hybridization was performed using a proprietary high sensitivity RNA amplification and detection technology (RNAscope, Advanced Cell Diagnostics), according to the manufacturer's instructions using the indicated proprietary probes and the RNAscope 2.5 HD Duplex Reagent Kit. Following in situ hybridization, sections were counterstained with hematoxylin before analysis and imaging with a light microscope (Olympus BX53) and attached camera (Olympus DP73). Proprietary (Advanced Cell Diagnostics) probes used were: Human, Hs-CXCL17 (513241) and Hs-C10orf99-C2 (437401-C2).

Immunofluorescence studies

In vivo localization of *Gpr25*- and co-injected control vector-transduced T cells: Recipient mice were injected retro-orbitally with 25 µg of fluorescently labeled anti-mouse CD31 antibody (DyLight 633, clone 390, InvivoMab) 15 minutes prior to sacrifice. Before organ harvest, the lungs were inflated with a 50% OCT (Sakura® Finetek) solution in PBS. Immediately after organ removal, the trachea, uterine horn, gallbladder, and PLN were gently compressed to a thickness of approximately 10-30 µm on a glass slide. Alternatively, the stomach, lung, tongue, small intestine, and colon were snap-frozen in OCT on dry ice and stored at −80°C for subsequent preparation of 10 µm cryosections.

Immunofluorescence quantification of endogenous T cells: The mice were anesthetized and transcardially perfused with PBS. The lungs were inflated with a 50% OCT solution in PBS. Tissues were harvested and fixed in 4% PFA for one hour, washed in PBS, and incubated in 30% sucrose for 24 hours at 4°C slowly shaking. Tissues were then embedded in OCT, flash frozen on dry ice, stored at -80°C and cut into 10 µm cryosections. On the day of staining, slides were thawed, washed consecutively in PBST (0.4% TWEEN® 20, 4% BSA in PBS). Slides were blocked in blocking buffer (2% goat serum, 0.3 % triton in PBS). Slides were then incubated overnight at 4C with conjugated antibodies APC-anti mouse TCRβ (clone H57-597, 1:50 dilution), from Biolegend; PE-anti mouse CD103 (clone 2E7, 1:50 dilution) from Biolegend, as well as the following primary antibodies; anti mouse CD8α (clone 4SM15, 1:100 dilution) from Invitrogen or the anti mouse CD4 (clone RM4-5, 1:100 dilution) from Biolegend. Slides were then washed in PBST 3 times for 10 mins followed with blocking with 5% of mouse serum for 10 mins. Slides were then incubated with goat anti-rat IgG cross-adsorbed AF488 secondary antibody (1:50 dilution) from Invitrogen for 45 mins at room temperature. Slides were then washed in PBST 3 times for 10 mins and closed with Fluoromount-G (Southern Biotech).

Imaging was conducted using a Nikon or Zeiss 880 confocal microscope, and quantification of T cells was performed using Imaris software.

For Figure 6 G and H, T cell counts were normalized in each section to the cross-sectional area of epithelium in all organs, and the area of peri-bronchial interstitium and free alveolar interstitium counted in lung,

determined in ImageJ after outlining the indicated areas. Sections were counted unblinded by two individuals. As validation, a third individual counted representative sections single blind.

Immunohistochemistry studies

Human cerebella were from post-mortem tissue, formalin fixed and embedded in paraffin via standard methods. After deparaffinization and re-hydration to water, slides were placed in 3% hydrogen peroxide for 15 minutes to quench endogenous peroxidase. 10mM citric acid (pH6) was used for antigen retrieval for 25 minutes at 95C. Normal goat serum was used for 30 min at room temperature to block unspecific binding before overnight incubation at 4C with the primary anti-human CXCL17 (clone 422204, R&D) or isotype control (clone G3A1 mouse IgG1, Cell Signaling) antibodies. Next, the secondary polymerized goat anti mouse IgG ImmPRESS (peroxidase) kit from Vectorlabs was used. Finally, sections were rehydrated in ethanols, and cleared in xylenes before coverslipping with synthetic mounting media. In Extended Data Figure 9 DAB is shown in images without counterstain. Images were captured with an slide digital scanner Aperio AT2 operated with the v12.4.3.5008 software.

Data and statistical analysis

Results are expressed as mean ± SEM and individual data points represent biological or technical replicates as specified, with the exception of Fig 3H where data (n=2 per condition) are presented as mean in agreement with the journal guidance. To test whether *GPR25* expression is dependent on cell type, tissue type and/or disease state in scRNA analyses, we calculated the mean of single-cell *GPR25* expression per sample per condition, and modeled *GPR25* mean against subset, tissue and their interaction (Figure 2E), or against subset, disease and their interaction (Extended Data Figure 2 and 8A) in linear regression models. *P*-value tests for the null hypothesis that the groups being compared have no effect on *GPR25* level. Statistical difference of endogenous T cells in the indicated environments in WT vs *Cxcl17*-/- mice was tested using bivariate linear regression modeling cell counts against replicate animals and genotype (Figure 6G and H).

Statistics for Figure 6B imaging analyses were performed using Fisher's exact test in R, comparing pooled cell counts per condition. For other experiments, we used GraphPad Prism as indicated in the corresponding figure legends. Differences were considered significant at $P < 0.05$.

Extended data figure legends

Extended Data Figure 1. Tissue- and subset-selective expression of *GPR25* by lymphocytes
A. Comparison of *GPR25*, *GPR15* and *CCR9* in the airway, colon, and SI, respectively, in total CD4 or CD8 T cells. Data from healthy adult and pediatric donors (n=12-16). Boxplots of *GPR25*, *GPR15* and *CCR9* mean imputed expression per patient sample in total CD4 or CD8 T cells are shown, with each dot representing the mean value per sample. Hinges of box correspond to the first and third quartiles. Whisker extends from the corresponding hinge to the max/min value no further than 1.5x interquartile range from the hinge. Samples with fewer than 10 cells are not plotted. *: *p*-value < 0.05; ****: *p*-value < 0.0001, two-tailed T-test.
B. Normalized transcript per million (TPM) of *GPR25* from scRNAseq of all human cell types from the Human Protein Atlas.
C. Mean TPM of *GPR25* from bulk RNAseq of immune cell types sorted from PBMC of 4 healthy donors. Sample source information is provided in Supplementary Table 1.

Extended Data Figure 2. *GPR25* expression and association with neurodegeneration
scRNAseq violin plots of imputed *GPR25* expression in T cell subsets and myeloid cells in CSF samples from healthy donors and patients with mild cognitive impairment/Alzheimer's Disease (MCI/AD). Data from all patients with more than 1000 cells are presented with means of individual donors (open circles) and mean values of the donor means (solid circles) ± SEM (n=28). *: *p*-value < 0.05; **: *p*-value < 0.01; ****: *p*-value < 0.0001; n.s.: non-significant, multivariate regression. Trending differences between healthy and diseased samples are not statistically significant. Sample source information is provided in Supplementary Table 1

Extended Data Figure 3. Expression of *GPR25* in T cells in the MLN, TLN and small intestines.
A. *GPR25+* cells are enriched in mature Tregs during CD4 T cell differentiation in MLN and TLN. CD4 T cells aligned along a developmental path from CD4 naive cells illustrating sequential expression of *CCR9* and *GPR25* by T cells along a developmental (pseudotime) trajectory seeded from naive CD4 cells. Mature *FOXP3*-high *IL2RA*-hi Tregs (Treg hi) emerge late and are enriched in *GPR25+CCR9+* cells in MLN. Cells are pooled from 14 MLN and 9 TLN samples from healthy donors.
B. *GPR25* is expressed by subsets of Treg and TEM in the small intestines. Violin plots illustrating *CCR9* and *GPR15* expression by *GPR25+* (*GPR25* > 0.2) vs *GPR25-* (*GPR25* < 0.2) T cells in SI, pooled from 12 healthy donors and presented with means of individual donors (open circles) and mean values of donor means (solid circles) ± SEM. All gene expression imputed. Sample source information is provided in Supplementary Table 1.

Extended Data Figure 4. Predicted structure of the GPR25 complex with CXCL17.
A. The overall view of the complex. Receptor and the CXCL17 C-terminal helix are shown in white and black ribbons, respectively, and viewed along the plane of the membrane.
B. The acidic C-terminus of CXCL17 is predicted to insert into the predominantly positively charged orthosteric binding pocket of GPR25. The receptor is viewed along the plane of the membrane as in (**A**) and is shown as a cut-away space-filling mesh colored by electrostatic potential (blue: positive, red: negative). The C-terminal part of CXCL17 is shown as black ribbon (backbone) and sticks (for the carboxyl group and residue side-chains only).
C. The amino-acid residue environment in the receptor binding pocket is complementary to the molecular composition of the distal C-terminus of CXCL17, which ensures favorable hydrophobic packing against $W95^{2.60}$ and prominent hydrogen bonding interactions with the network of $S116^{3.29}$, $R178^{4.64}$, $E193^{45.52}$, and $R264^{6.55}$. Receptor is viewed across the plane of the membrane from the extracellular side and shown in white ribbon and sticks; the two C-terminal residues of CXCL17 are shown in black. Cyan dotted lines denote hydrogen bonds.
The model was built using AlphaFold 2.3.2 Multimer[88-90]. Structure was refined and visualized in ICM 3.9-3b[91].

Extended Data Figure 5. CXCL17 is a chemoattractant ligand for GPR25 but not GPR15 or CMKLR1.
A. Human GPR15 transfectants migration to GPR15LG (250nM) and CXCL17 (10-300nM). **B**. Human CMKLR1 transfectants migration to chemerin and CXCL17 (10-300nM). **C**. Checkerboard assay with human 4CysCXCL17 250nM and human GPR25 transfectants. **D**. Pertussis toxin (100 ng/ml, 2 hours pre-treatment before migration assay) inhibits CXCL17-induced chemotaxis on human GPR25 L1-2 transfectants. **E**. Intact mouse 6CysCXCL17 (3nM - 1μM) is an active chemoattractant on human GPR25. **F**. Intact human

4CysCXCL17 is an active chemoattractant on mouse GPR25. **G**. mGPR25 transduced cells, but not the empty vector transduced counterparts robustly chemotax to mouse and human CXCL17 in *in vitro* transwell-based migration assays. Results with 3-9 replicates pooled from at least two independent experiments are shown as mean ± SEM. ****; P<0.0001 vs no chemokine control in a two-tailed T-test.

Extended Data Figure 6. Subset selective T cell chemotaxis to CXCL17. **A**. Table showing % of migration to no chemokine in Figure 4A and C. **B-D**. Tonsil cells were migrated in transwells to human 4CysCXCL17 or human GPR15L for 3 hrs. Migrated and input cells were counted and phenotyped by flow cytometry. **B-D**. Naive (CD45RO- CD45RA+) or indicated effector/memory (CD45RO+ CD45RA-) TCRαβ+ CD4+ subsets were defined with MAbs to intracellular Foxp3 and CD25 (Tregs), and CD161, a marker of mucosal tissue homing T cells. Mucosal-associated invariant T cells are Vα7.2+. NK cells were defined as CD14-, HLA/DR-, CD3-, CD19-, CD56+, CD16-. NKT shared the same immunophenotyping but were gated as CD3+. Conventional dendritic cells (DC) were defined as CD3-, CD19-, CD14-, HLA/DR+, CD11c+. Plasmacytoid dendritic cells (pDC) were defined as CD3-, CD19-, CD14-, HLA/DR+, CD123+. Data are % of input cells migrated above mean "no chemokine/NC control" migration (which defines 0). **E**. Table showing % of migration to no chemokine in panels B-D. Results pooled from three independent experiments and shown as mean ± SEM of % of specific migration, except for hGPR15LG (two experiments). N ≥ 5. *; P<0.05, **; p<0.01, ***; p<0.001, ****; p<0.0001. One way ANOVA analysis with Dunnet post hoc test was performed to each cell subset comparing the indicated condition vs no chemokine control (NC).

Extended Data Figure 7. *CXCL17* expression in the human and mouse CNS.

A. UMAP of scRNAseq data of the human brain from Human Protein Atlas. Cells with *CXCL17* expression are denoted in black.

B. Violin plots illustrating *CXCL17* expression by subsets in the hippocampus from healthy donors (n=2).

C. Violin plots of *Cxcl17* expression by CNS cells from whole brains of mice at 4-week (n=2) or 90-week (n=2).

D. Violin plots of *Cxcl17* in mouse spinal cord subsets in injury models (n=3). In B-D mean imputed expression values from individual donors (open circles) and mean values of the donor means (solid circles) are shown with SEM. Sample source information is provided in Supplementary Table 1.

Extended Data Figure 8. *CXCL17* expression in the airway and the gut.

A. Violin plots showing *CXCL17* expression in airway epithelial populations of healthy donors and COVID-19 patients. *: *p*-value < 0.05; **: *p*-value < 0.01; ***: *p*-value < 0.001, multivariate regression between healthy and severe COVID-19 samples.

B. Violin plots illustrating low expression level of *CXCL17* in the gut of healthy donors. Selective expression of *GPR15LG* in colon and *CCL25* in SI are shown for comparison. Mean imputed expression values from individual donors (open circles) and mean values of the donor means (solid circles) are shown with SEM. Sample source information is provided in Supplementary Table 1.

Extended Data Figure 9. CXCL17 immunohistology of the human cerebellum.

A. CXCL17 immunoreactivity highlights granule neurons (g). **B.** Reactivity of Purkinje (P) neurons and white matter (wm) surrounding a vessel (v). Methods: Sections of formalin fixed paraffin embedded normal human cerebellum were processed for antigen retrieval and staining with monoclonal mouse IgG anti-human CXCL17 (clone 422204, R&D) using the polymerized goat anti mouse IgG ImmPRESS (peroxidase) kit. DAB shown without counterstain. Isotype control (clone G3A1 mouse IgG1, Cell Signaling) is shown as inset in A. Results representative of 3 or more sections from 2 independent donors.

References in main text

1 Kunkel, E. J. & Butcher, E. C. Chemokines and the tissue-specific migration of lymphocytes. *Immunity* **16**, 1-4, doi:10.1016/s1074-7613(01)00261-8 (2002).

2 Ocon, B. *et al.* A Mucosal and Cutaneous Chemokine Ligand for the Lymphocyte Chemoattractant Receptor GPR15. *Front Immunol* **8**, 1111, doi:10.3389/fimmu.2017.01111 (2017).

3 Ricaño-Ponce, I. *et al.* Refined mapping of autoimmune disease associated genetic variants with gene expression suggests an important role for non-coding RNAs. *J Autoimmun* **68**, 62-74, doi:10.1016/j.jaut.2016.01.002 (2016).

4 Robinson, P. C. *et al.* Genetic dissection of acute anterior uveitis reveals similarities and differences in associations observed with ankylosing spondylitis. *Arthritis Rheumatol* **67**, 140-151, doi:10.1002/art.38873 (2015).

5 Habtezion, A., Nguyen, L. P., Hadeiba, H. & Butcher, E. C. Leukocyte Trafficking to the Small Intestine and Colon. *Gastroenterology* **150**, 340-354, doi:10.1053/j.gastro.2015.10.046 (2016).

6 Imaoka, K. *et al.* Nasal immunization of nonhuman primates with simian immunodeficiency virus p55gag and cholera toxin adjuvant induces Th1/Th2 help for virus-specific immune responses in reproductive tissues. *J Immunol* **161**, 5952-5958 (1998).

7 Sato, A. *et al.* Vaginal memory T cells induced by intranasal vaccination are critical for protective T cell recruitment and prevention of genital HSV-2 disease. *J Virol* **88**, 13699-13708, doi:10.1128/jvi.02279-14 (2014).

8 Stary, G. *et al.* VACCINES. A mucosal vaccine against Chlamydia trachomatis generates two waves of protective memory T cells. *Science* **348**, aaa8205, doi:10.1126/science.aaa8205 (2015).

9 Labuda, J. C. *et al.* Circulating immunity protects the female reproductive tract from Chlamydia infection. *Proc Natl Acad Sci U S A* **118**, doi:10.1073/pnas.2104407118 (2021).

10 Tordesillas, L. & Berin, M. C. Mechanisms of Oral Tolerance. *Clin Rev Allergy Immunol* **55**, 107-117, doi:10.1007/s12016-018-8680-5 (2018).

11 Choi, J. *et al.* T(REG)king From Gut to Brain: The Control of Regulatory T Cells Along the Gut-Brain Axis. *Front Immunol* **13**, 916066, doi:10.3389/fimmu.2022.916066 (2022).

12 Ellwardt, E., Walsh, J. T., Kipnis, J. & Zipp, F. Understanding the Role of T Cells in CNS Homeostasis. *Trends in Immunology* **37**, 154-165, doi:https://doi.org/10.1016/j.it.2015.12.008 (2016).

13 Hu, D. & Weiner, H. L. Unraveling the dual nature of brain CD8+ T cells in Alzheimer's disease. *Molecular Neurodegeneration* **19**, 16, doi:10.1186/s13024-024-00706-y (2024).

14 Pan, S. *et al.* Brain Catalog: a comprehensive resource for the genetic landscape of brain-related traits. *Nucleic Acids Res* **51**, D835-d844, doi:10.1093/nar/gkac895 (2023).

15 Park, J. E. *et al.* A cell atlas of human thymic development defines T cell repertoire formation. *Science* **367**, doi:10.1126/science.aay3224 (2020).

16 Billiet, L. *et al.* Single-cell profiling identifies a novel human polyclonal unconventional T cell lineage. *J Exp Med* **220**, doi:10.1084/jem.20220942 (2023).

17 Dermadi, D. *et al.* Exploration of Cell Development Pathways through High-Dimensional Single Cell Analysis in Trajectory Space. *iScience* **23**, 100842, doi:10.1016/j.isci.2020.100842 (2020).

18 Gao, X. & Cockburn, I. A. The development and function of CD11c(+) atypical B cells - insights from single cell analysis. *Front Immunol* **13**, 979060, doi:10.3389/fimmu.2022.979060 (2022).

19 Sigmundsdottir, H. & Butcher, E. C. Environmental cues, dendritic cells and the programming of tissue-selective lymphocyte trafficking. *Nat Immunol* **9**, 981-987, doi:10.1038/ni.f.208 (2008).

20 Swaminathan, G. *et al.* The aryl hydrocarbon receptor regulates expression of mucosal trafficking receptor GPR15. *Mucosal Immunol* **14**, 852-861, doi:10.1038/s41385-021-00390-x (2021).

21 Xiong, L. *et al.* Ahr-Foxp3-RORγt axis controls gut homing of CD4(+) T cells by regulating GPR15. *Sci Immunol* **5**, doi:10.1126/sciimmunol.aaz7277 (2020).

22 Mikhak, Z., Strassner, J. P. & Luster, A. D. Lung dendritic cells imprint T cell lung homing and promote lung immunity through the chemokine receptor CCR4. *Journal of Experimental Medicine* **210**, 1855-1869, doi:10.1084/jem.20130091 (2013).
23 Aleotti, A., Goulty, M., Lewis, C., Giorgini, F. & Feuda, R. The origin, evolution, and molecular diversity of the chemokine system. *Life Sci Alliance* **7**, doi:10.26508/lsa.202302471 (2024).
24 Ngo, T. *et al.* RETRACTED ARTICLE: Orphan receptor ligand discovery by pickpocketing pharmacological neighbors. *Nature Chemical Biology* **13**, 235-242, doi:10.1038/nchembio.2266 (2017).
25 Lee, W. Y., Wang, C. J., Lin, T. Y., Hsiao, C. L. & Luo, C. W. CXCL17, an orphan chemokine, acts as a novel angiogenic and anti-inflammatory factor. *Am J Physiol Endocrinol Metab* **304**, E32-40, doi:10.1152/ajpendo.00083.2012 (2013).
26 Burkhardt, A. M. *et al.* CXCL17 Is a Mucosal Chemokine Elevated in Idiopathic Pulmonary Fibrosis That Exhibits Broad Antimicrobial Activity. *The Journal of Immunology* **188**, 6399-6406, doi:10.4049/jimmunol.1102903 (2012).
27 Weinstein, E. J. *et al.* VCC-1, a novel chemokine, promotes tumor growth. *Biochemical and Biophysical Research Communications* **350**, 74-81, doi:https://doi.org/10.1016/j.bbrc.2006.08.194 (2006).
28 Pisabarro, M. T. *et al.* Cutting edge: novel human dendritic cell- and monocyte-attracting chemokine-like protein identified by fold recognition methods. *J Immunol* **176**, 2069-2073, doi:10.4049/jimmunol.176.4.2069 (2006).
29 Choreño-Parra, J. A., Thirunavukkarasu, S., Zúñiga, J. & Khader, S. A. The protective and pathogenic roles of CXCL17 in human health and disease: Potential in respiratory medicine. *Cytokine Growth Factor Rev* **53**, 53-62, doi:10.1016/j.cytogfr.2020.04.004 (2020).
30 Giblin, S. P. & Pease, J. E. What defines a chemokine? - The curious case of CXCL17. *Cytokine* **168**, 156224, doi:10.1016/j.cyto.2023.156224 (2023).
31 Oka, T. *et al.* CXCL17 Attenuates Imiquimod-Induced Psoriasis-like Skin Inflammation by Recruiting Myeloid-Derived Suppressor Cells and Regulatory T Cells. *The Journal of Immunology* **198**, 3897-3908, doi:10.4049/jimmunol.1601607 (2017).
32 Binti Mohd Amir, N. A. S. *et al.* Evidence for the Existence of a CXCL17 Receptor Distinct from GPR35. *J Immunol* **201**, 714-724, doi:10.4049/jimmunol.1700884 (2018).
33 Park, S.-J., Lee, S.-J., Nam, S.-Y. & Im, D.-S. GPR35 mediates lodoxamide-induced migration inhibitory response but not CXCL17-induced migration stimulatory response in THP-1 cells; is GPR35 a receptor for CXCL17? *British Journal of Pharmacology* **175**, 154-161, doi:https://doi.org/10.1111/bph.14082 (2018).
34 Ding, J. *et al.* CXCL17 induces activation of human mast cells via MRGPRX2. *Allergy* **n/a**, doi:https://doi.org/10.1111/all.16036.
35 White, C. W. *et al.* CXCL17 is an allosteric inhibitor of CXCR4 through a mechanism of action involving glycosaminoglycans. *Sci Signal* **17**, eabl3758, doi:10.1126/scisignal.abl3758 (2024).
36 Laudanna, C., Campbell, J. J. & Butcher, E. C. Role of Rho in chemoattractant-activated leukocyte adhesion through integrins. *Science* **271**, 981-983, doi:10.1126/science.271.5251.981 (1996).
37 Wyrożemski, Ł. & Qiao, S.-W. Immunobiology and conflicting roles of the human CD161 receptor in T cells. *Scandinavian Journal of Immunology* **94**, e13090, doi:https://doi.org/10.1111/sji.13090 (2021).
38 Lazarus, N. H. *et al.* A common mucosal chemokine (mucosae-associated epithelial chemokine/CCL28) selectively attracts IgA plasmablasts. *J Immunol* **170**, 3799-3805, doi:10.4049/jimmunol.170.7.3799 (2003).
39 Srivastava, R. *et al.* CXCL17 Chemokine-Dependent Mobilization of CXCR8(+)CD8(+) Effector Memory and Tissue-Resident Memory T Cells in the Vaginal Mucosa Is Associated with Protection against Genital Herpes. *J Immunol* **200**, 2915-2926, doi:10.4049/jimmunol.1701474 (2018).
40 Hernández-Ruiz, M. *et al.* Cxcl17(-/-) mice develop exacerbated disease in a T cell-dependent autoimmune model. *J Leukoc Biol* **105**, 1027-1039, doi:10.1002/jlb.3a0918-345rr (2019).

41 Kim, J. *et al.* Spontaneous Proliferation of CD4(+) T Cells in RAG-Deficient Hosts Promotes Antigen-Independent but IL-2-Dependent Strong Proliferative Response of Naïve CD8(+) T Cells. *Front Immunol* **9**, 1907, doi:10.3389/fimmu.2018.01907 (2018).
42 Pruenster, M. *et al.* The Duffy antigen receptor for chemokines transports chemokines and supports their promigratory activity. *Nat Immunol* **10**, 101-108, doi:10.1038/ni.1675 (2009).
43 Wein, A. N. *et al.* CXCR6 regulates localization of tissue-resident memory CD8 T cells to the airways. *J Exp Med* **216**, 2748-2762, doi:10.1084/jem.20181308 (2019).
44 Schenkel, J. M. & Masopust, D. Tissue-resident memory T cells. *Immunity* **41**, 886-897, doi:10.1016/j.immuni.2014.12.007 (2014).
45 Ehrhardt, G. R. *et al.* Expression of the immunoregulatory molecule FcRH4 defines a distinctive tissue-based population of memory B cells. *J Exp Med* **202**, 783-791, doi:10.1084/jem.20050879 (2005).
46 Alon, R. *et al.* Leukocyte trafficking to the lungs and beyond: lessons from influenza for COVID-19. *Nat Rev Immunol* **21**, 49-64, doi:10.1038/s41577-020-00470-2 (2021).
47 Liu, J. Z. *et al.* Dense fine-mapping study identifies new susceptibility loci for primary biliary cirrhosis. *Nat Genet* **44**, 1137-1141, doi:10.1038/ng.2395 (2012).
48 Odoardi, F. *et al.* T cells become licensed in the lung to enter the central nervous system. *Nature* **488**, 675-679, doi:10.1038/nature11337 (2012).

References in Material and Methods, as well as Extended Data Figures

49 Kim, E., Tran, M., Sun, Y. & Huh, J. R. Isolation and analyses of lamina propria lymphocytes from mouse intestines. *STAR Protoc* **3**, 101366, doi:10.1016/j.xpro.2022.101366 (2022).
50 Steinert, E. M. *et al.* Quantifying Memory CD8 T Cells Reveals Regionalization of Immunosurveillance. *Cell* **161**, 737-749, doi:10.1016/j.cell.2015.03.031 (2015).
51 Cumba Garcia, L. M., Huseby Kelcher, A. M., Malo, C. S. & Johnson, A. J. Superior isolation of antigen-specific brain infiltrating T cells using manual homogenization technique. *J Immunol Methods* **439**, 23-28, doi:10.1016/j.jim.2016.09.002 (2016).
52 Sumida, H. *et al.* GPR55 regulates intraepithelial lymphocyte migration dynamics and susceptibility to intestinal damage. *Sci Immunol* **2**, doi:10.1126/sciimmunol.aao1135 (2017).
53 Allen, S. J., Hamel, D. J. & Handel, T. M. A rapid and efficient way to obtain modified chemokines for functional and biophysical studies. *Cytokine* **55**, 168-173, doi:10.1016/j.cyto.2011.05.002 (2011).
54 Lazar, G. A., Desjarlais, J. R. & Handel, T. M. De novo design of the hydrophobic core of ubiquitin. *Protein Sci* **6**, 1167-1178, doi:10.1002/pro.5560060605 (1997).
55 Zabel, B. A. *et al.* Chemerin activation by serine proteases of the coagulation, fibrinolytic, and inflammatory cascades. *J Biol Chem* **280**, 34661-34666, doi:10.1074/jbc.M504868200 (2005).
56 Honda, S. *et al.* Ligand-induced adhesion to activated endothelium and to vascular cell adhesion molecule-1 in lymphocytes transfected with the N-formyl peptide receptor. *The Journal of Immunology* **152**, 4026-4035, doi:10.4049/jimmunol.152.8.4026 (1994).
57 Sikkema, L. *et al.* An integrated cell atlas of the lung in health and disease. *Nat Med* **29**, 1563-1577, doi:10.1038/s41591-023-02327-2 (2023).
58 Yoshida, M. *et al.* Local and systemic responses to SARS-CoV-2 infection in children and adults. *Nature* **602**, 321-327, doi:10.1038/s41586-021-04345-x (2022).
59 Dominguez Conde, C. *et al.* Cross-tissue immune cell analysis reveals tissue-specific features in humans. *Science* **376**, eabl5197, doi:10.1126/science.abl5197 (2022).
60 He, P. *et al.* A human fetal lung cell atlas uncovers proximal-distal gradients of differentiation and key regulators of epithelial fates. *Cell* **185**, 4841-4860 e4825, doi:10.1016/j.cell.2022.11.005 (2022).
61 He, S. *et al.* Single-cell transcriptome profiling of an adult human cell atlas of 15 major organs. *Genome Biol* **21**, 294, doi:10.1186/s13059-020-02210-0 (2020).

62 Schalck, A. *et al.* Single-Cell Sequencing Reveals Trajectory of Tumor-Infiltrating Lymphocyte States in Pancreatic Cancer. *Cancer Discov* **12**, 2330-2349, doi:10.1158/2159-8290.CD-21-1248 (2022).
63 Chang, L. *et al.* Single-cell Clonal Tracing of Glandular and Circulating T cells identifies a population of CD9+CD8+T cells in primary Sjogren's Syndrome. *J Leukoc Biol*, doi:10.1093/jleuko/qiad071 (2023).
64 Piehl, N. *et al.* Cerebrospinal fluid immune dysregulation during healthy brain aging and cognitive impairment. *Cell* **185**, 5028-5039 e5013, doi:10.1016/j.cell.2022.11.019 (2022).
65 Peng, T. *et al.* Distinct populations of antigen-specific tissue-resident CD8+ T cells in human cervix mucosa. *JCI Insight* **6**, doi:10.1172/jci.insight.149950 (2021).
66 Elmentaite, R. *et al.* Cells of the human intestinal tract mapped across space and time. *Nature* **597**, 250-255, doi:10.1038/s41586-021-03852-1 (2021).
67 Saluzzo, S. *et al.* Delayed antiretroviral therapy in HIV-infected individuals leads to irreversible depletion of skin- and mucosa-resident memory T cells. *Immunity* **54**, 2842-2858 e2845, doi:10.1016/j.immuni.2021.10.021 (2021).
68 Karlsson, M. *et al.* A single-cell type transcriptomics map of human tissues. *Sci Adv* **7**, doi:10.1126/sciadv.abh2169 (2021).
69 Sjostedt, E. *et al.* An atlas of the protein-coding genes in the human, pig, and mouse brain. *Science* **367**, doi:10.1126/science.aay5947 (2020).
70 Siletti, K. *et al.* Transcriptomic diversity of cell types across the adult human brain. *Science* **382**, eadd7046, doi:10.1126/science.add7046 (2023).
71 Allen, W. E., Blosser, T. R., Sullivan, Z. A., Dulac, C. & Zhuang, X. Molecular and spatial signatures of mouse brain aging at single-cell resolution. *Cell* **186**, 194-208 e118, doi:10.1016/j.cell.2022.12.010 (2023).
72 Matson, K. J. E. *et al.* Single cell atlas of spinal cord injury in mice reveals a pro-regenerative signature in spinocerebellar neurons. *Nat Commun* **13**, 5628, doi:10.1038/s41467-022-33184-1 (2022).
73 Hao, Y. *et al.* Integrated analysis of multimodal single-cell data. *Cell* **184**, 3573-3587.e3529, doi:10.1016/j.cell.2021.04.048 (2021).
74 Hao, Y. *et al.* Dictionary learning for integrative, multimodal and scalable single-cell analysis. *Nat Biotechnol* **42**, 293-304, doi:10.1038/s41587-023-01767-y (2024).
75 Lun, A. T., McCarthy, D. J. & Marioni, J. C. A step-by-step workflow for low-level analysis of single-cell RNA-seq data with Bioconductor. *F1000Res* **5**, 2122, doi:10.12688/f1000research.9501.2 (2016).
76 McCarthy, D. J., Campbell, K. R., Lun, A. T. & Wills, Q. F. Scater: pre-processing, quality control, normalization and visualization of single-cell RNA-seq data in R. *Bioinformatics* **33**, 1179-1186, doi:10.1093/bioinformatics/btw777 (2017).
77 Haghverdi, L., Lun, A. T. L., Morgan, M. D. & Marioni, J. C. Batch effects in single-cell RNA-sequencing data are corrected by matching mutual nearest neighbors. *Nat Biotechnol* **36**, 421-427, doi:10.1038/nbt.4091 (2018).
78 Lim, H. S. & Qiu, P. Quantifying Cell-Type-Specific Differences of Single-Cell Datasets Using Uniform Manifold Approximation and Projection for Dimension Reduction and Shapley Additive exPlanations. *J Comput Biol* **30**, 738-750, doi:10.1089/cmb.2022.0366 (2023).
79 van Dijk, D. *et al.* Recovering Gene Interactions from Single-Cell Data Using Data Diffusion. *Cell* **174**, 716-729 e727, doi:10.1016/j.cell.2018.05.061 (2018).
80 King, H. W. *et al.* Single-cell analysis of human B cell maturation predicts how antibody class switching shapes selection dynamics. *Sci Immunol* **6**, doi:10.1126/sciimmunol.abe6291 (2021).
81 Monaco, G. *et al.* RNA-Seq Signatures Normalized by mRNA Abundance Allow Absolute Deconvolution of Human Immune Cell Types. *Cell Rep* **26**, 1627-1640 e1627, doi:10.1016/j.celrep.2019.01.041 (2019).
82 Ngo, T. *et al.* Orphan receptor ligand discovery by pickpocketing pharmacological neighbors. *Nat Chem Biol* **13**, 235-242, doi:10.1038/nchembio.2266 (2017).
83 Uhlen, M. *et al.* The human secretome. *Sci Signal* **12**, doi:10.1126/scisignal.aaz0274 (2019).

84 Kinsella, R. J. *et al.* Ensembl BioMarts: a hub for data retrieval across taxonomic space. *Database (Oxford)* **2011**, bar030, doi:10.1093/database/bar030 (2011).
85 Altschul, S. F. *et al.* Gapped BLAST and PSI-BLAST: a new generation of protein database search programs. *Nucleic Acids Res* **25**, 3389-3402, doi:10.1093/nar/25.17.3389 (1997).
86 Shiryev, S. A., Papadopoulos, J. S., Schaffer, A. A. & Agarwala, R. Improved BLAST searches using longer words for protein seeding. *Bioinformatics* **23**, 2949-2951, doi:10.1093/bioinformatics/btm479 (2007).
87 Uhlen, M. *et al.* Proteomics. Tissue-based map of the human proteome. *Science* **347**, 1260419, doi:10.1126/science.1260419 (2015).
88 Evans, R. *et al.* Protein complex prediction with AlphaFold-Multimer. *bioRxiv*, 2021.2010.2004.463034, doi:10.1101/2021.10.04.463034 (2022).
89 Jumper, J. *et al.* Highly accurate protein structure prediction with AlphaFold. *Nature* **596**, 583-589, doi:10.1038/s41586-021-03819-2 (2021).
90 Senior, A. W. *et al.* Improved protein structure prediction using potentials from deep learning. *Nature* **577**, 706-710, doi:10.1038/s41586-019-1923-7 (2020).
91 Abagyan, R. & Totrov, M. Biased probability Monte Carlo conformational searches and electrostatic calculations for peptides and proteins. *J Mol Biol* **235**, 983-1002, doi:10.1006/jmbi.1994.1052 (1994).

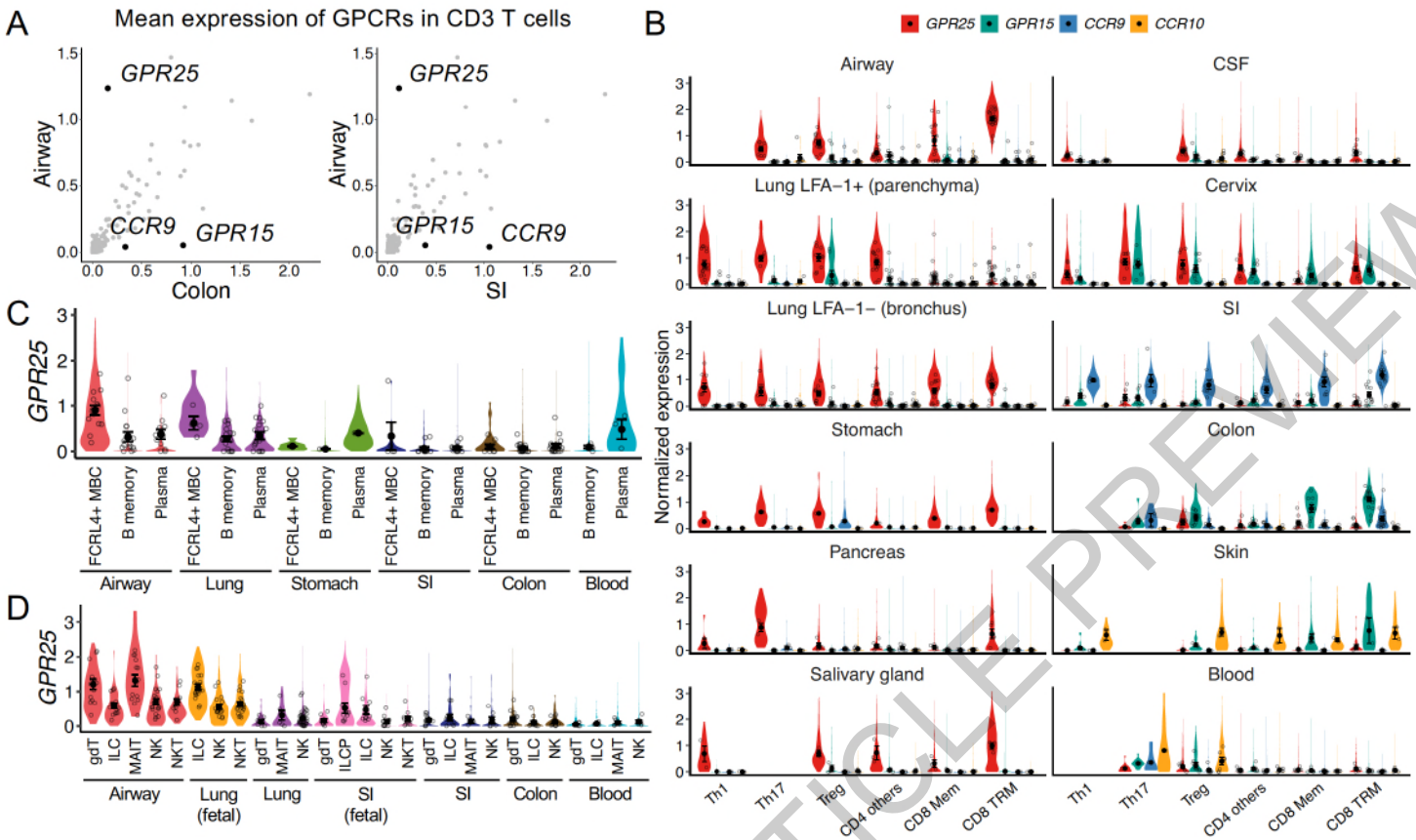

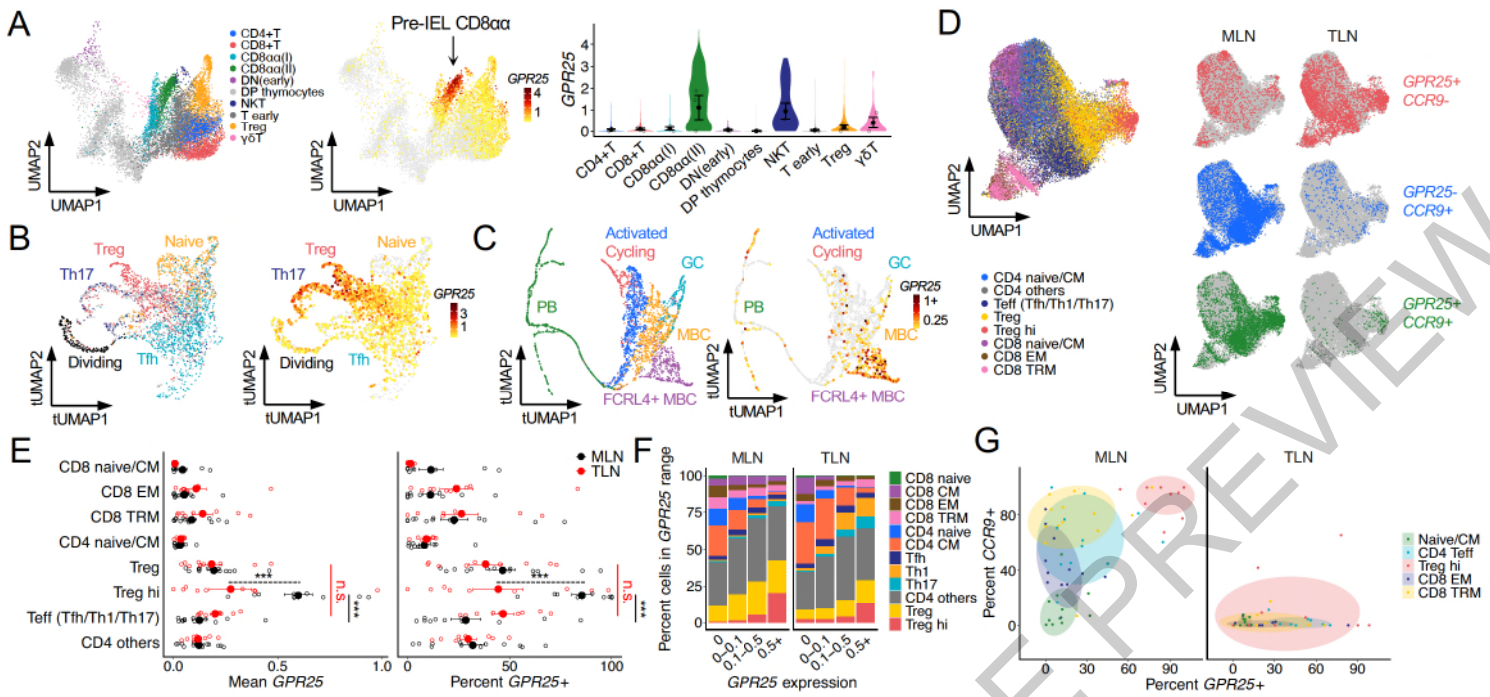

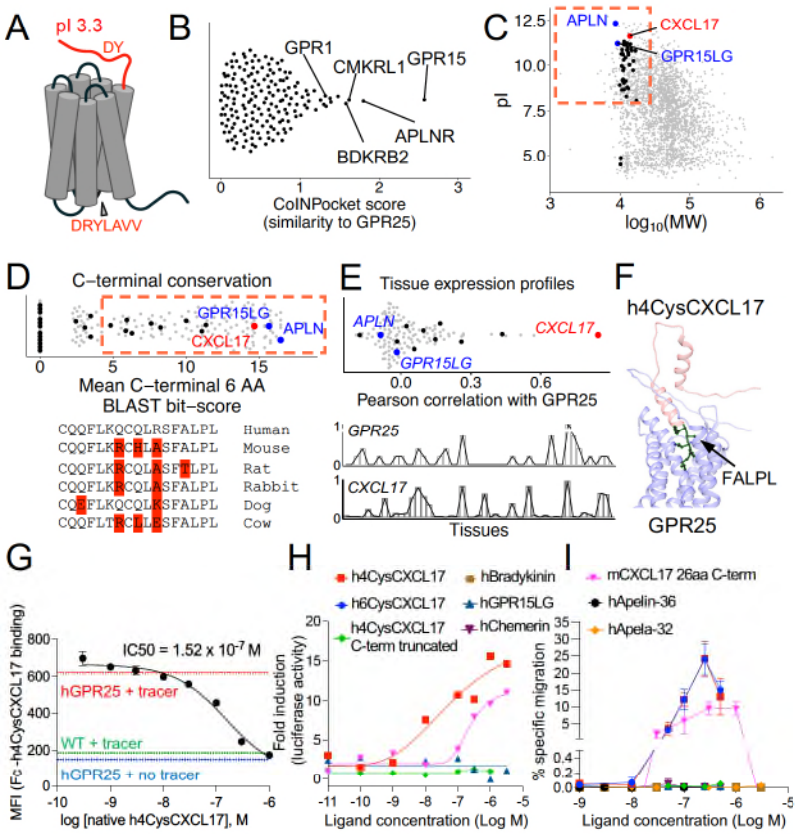

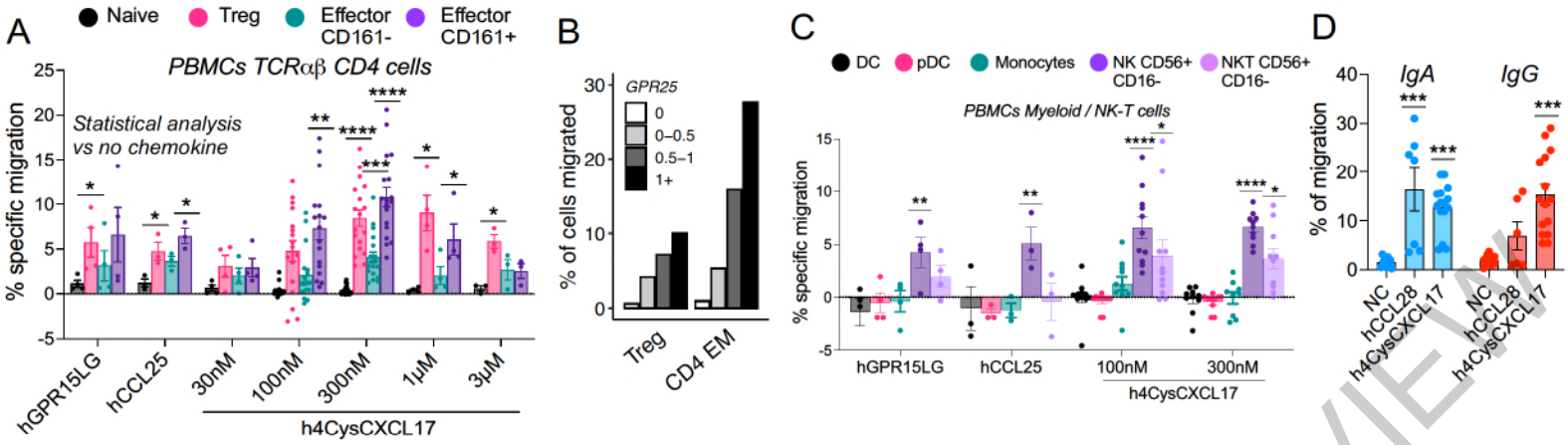

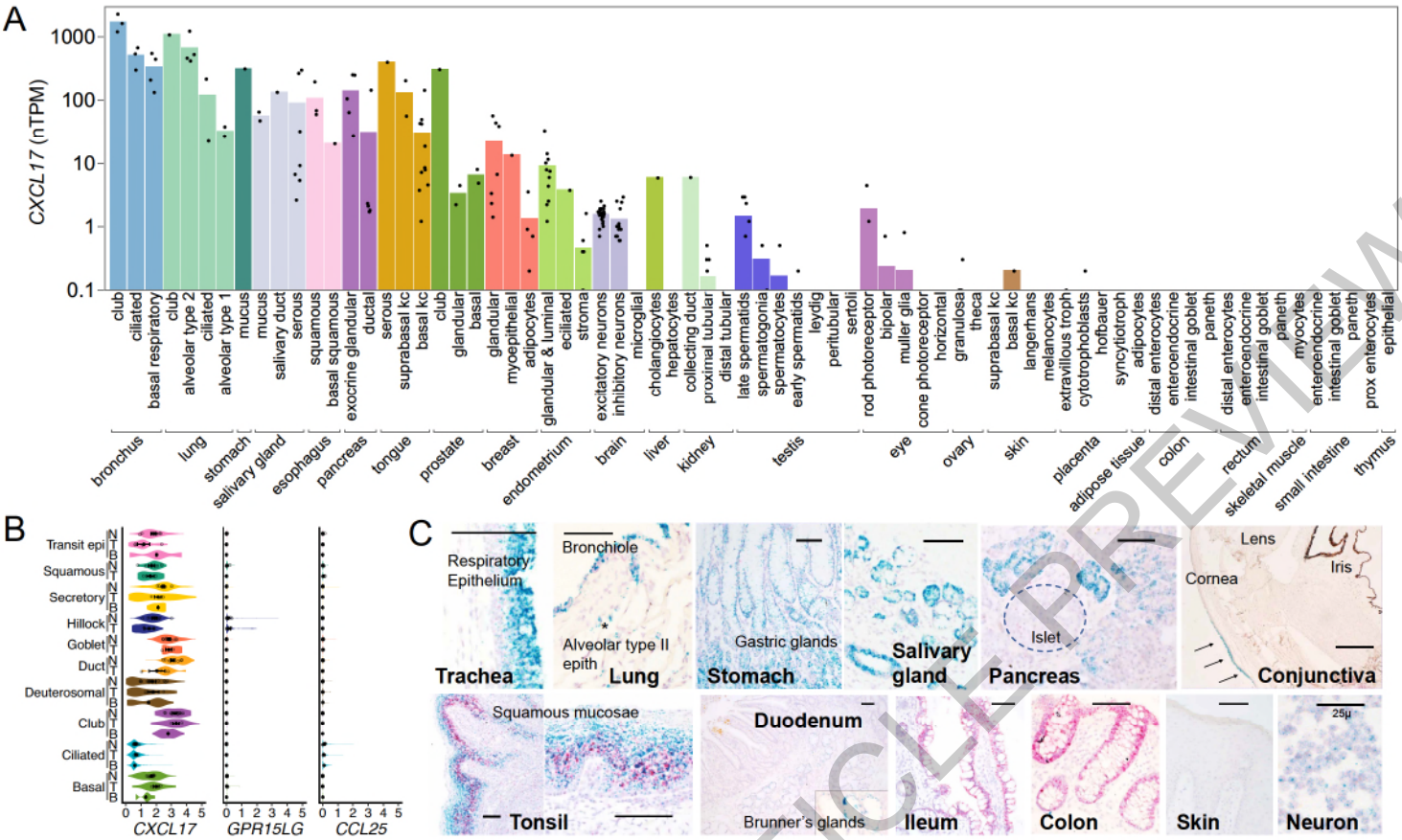

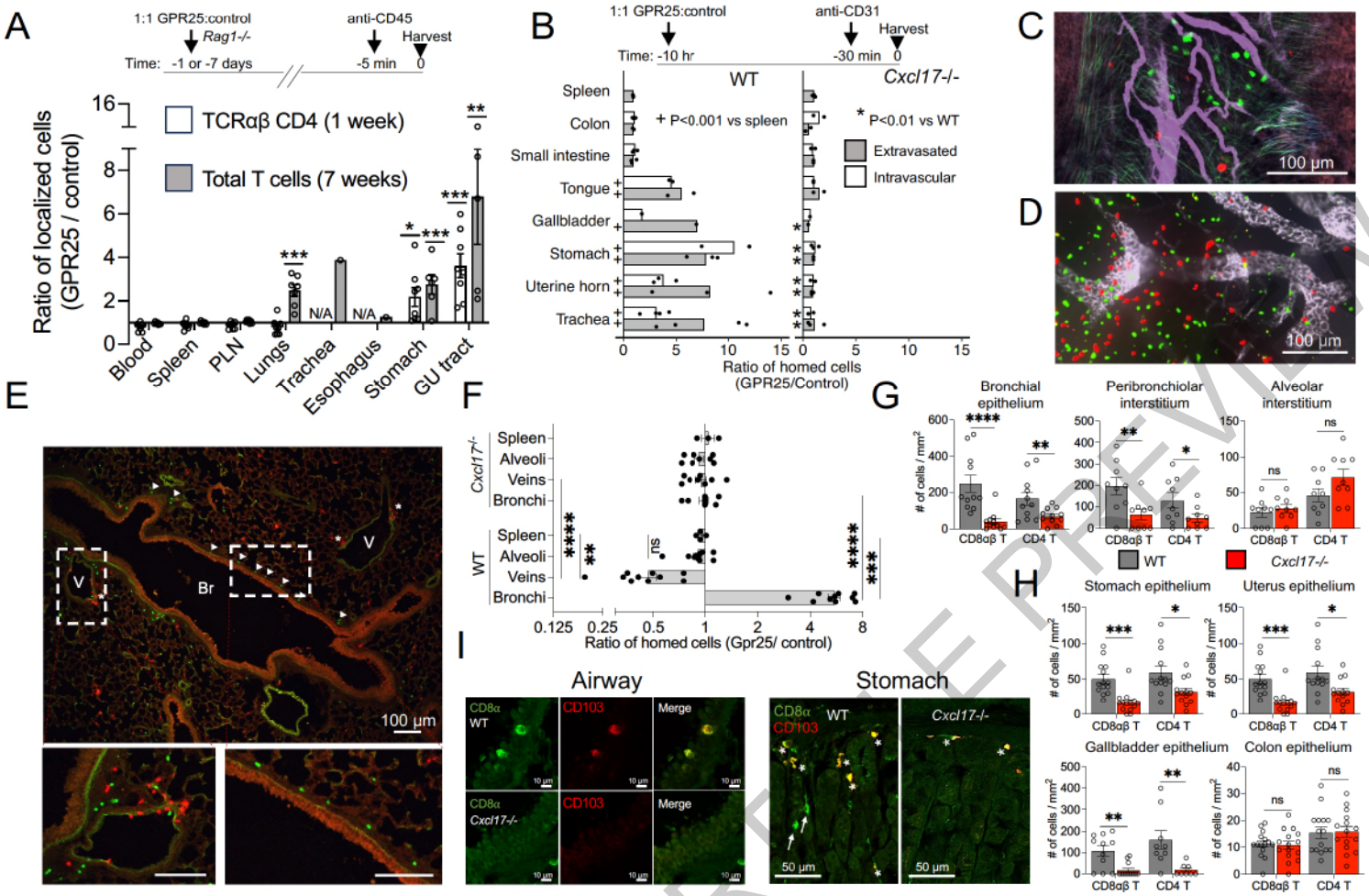

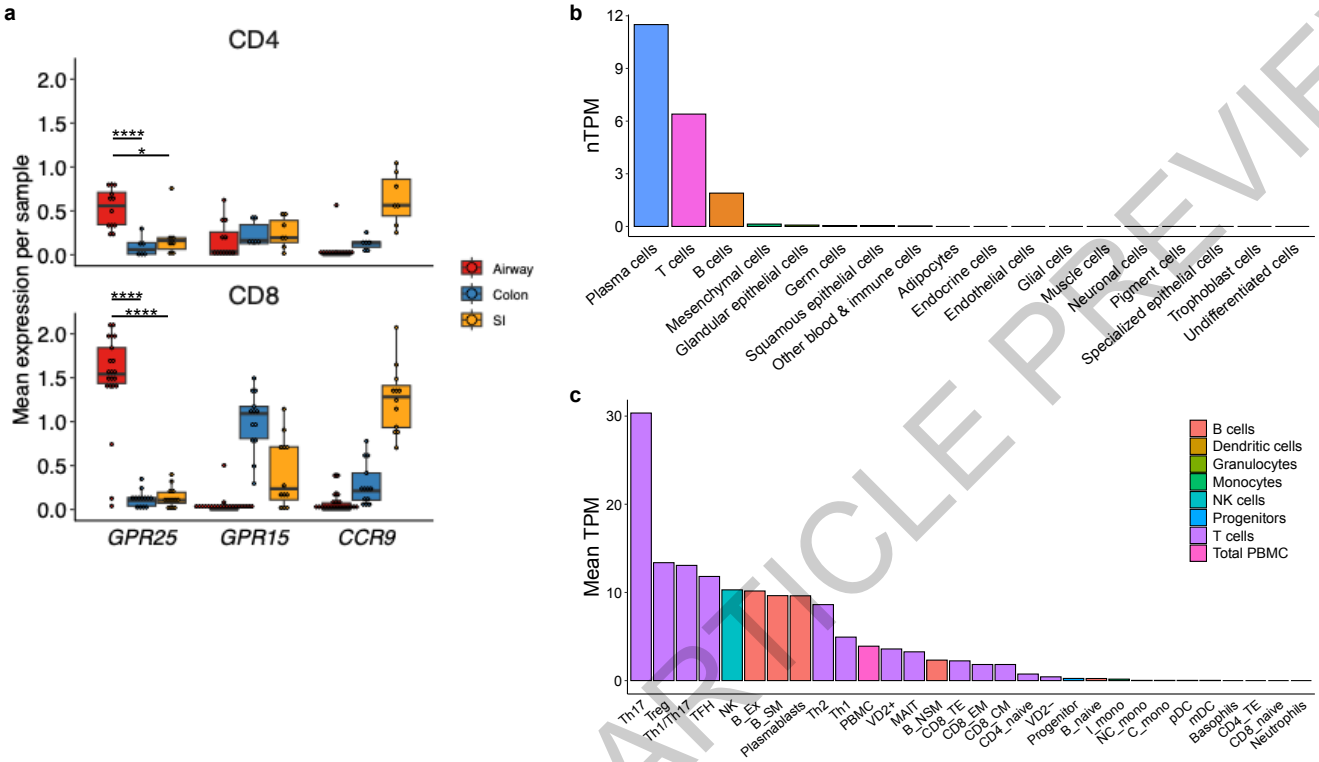

Extended Data Fig. 1

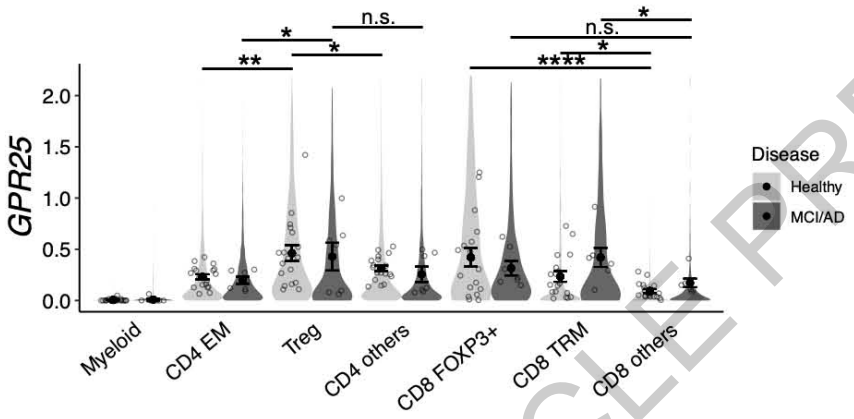

Extended Data Fig. 2

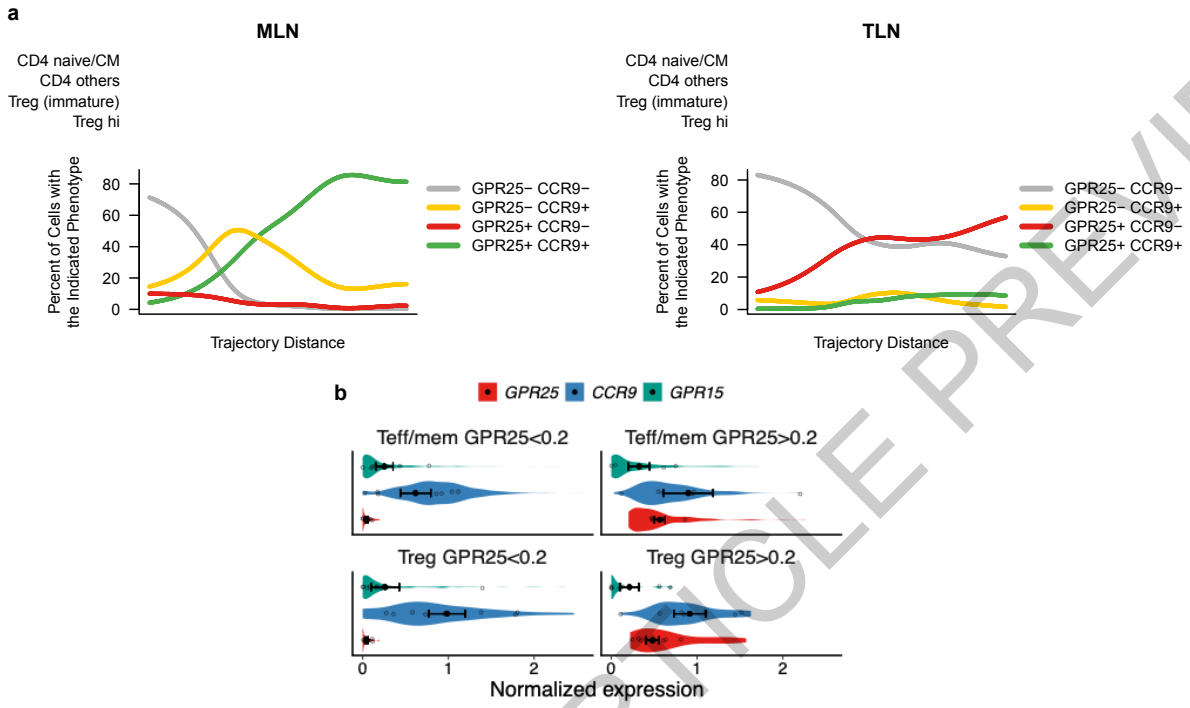

Extended Data Fig. 3

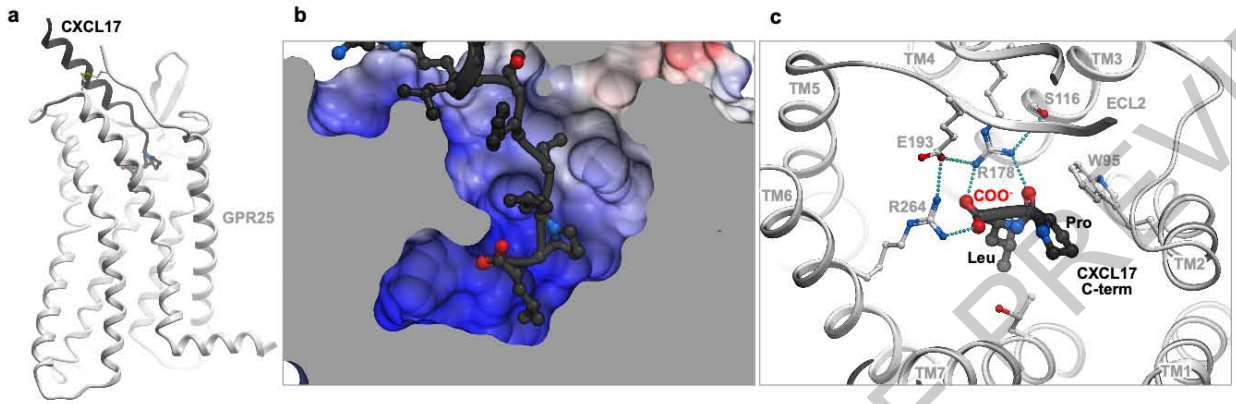

Extended Data Fig. 4

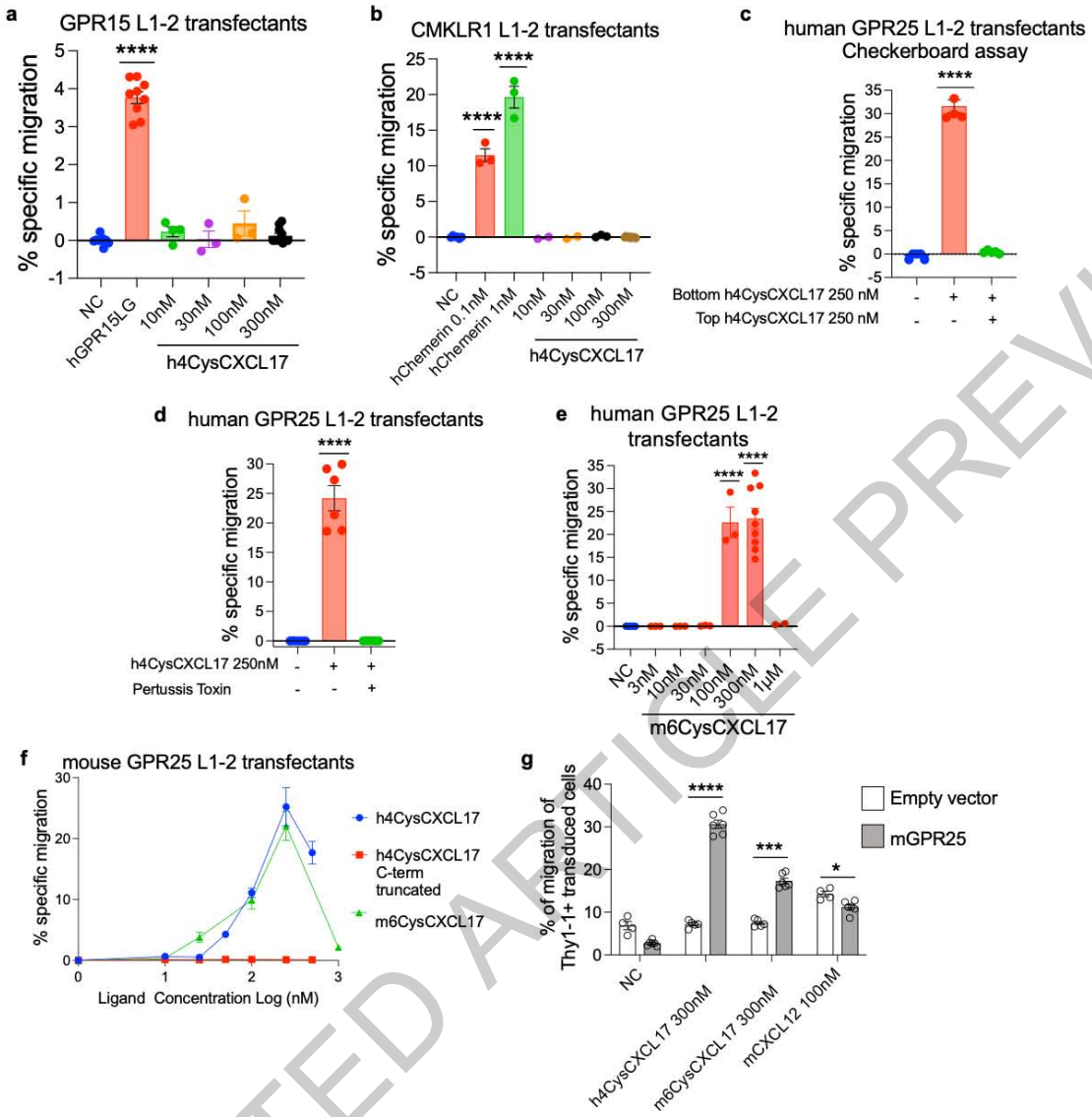

Extended Data Fig. 5

a

Figure 4A subsets	Mean ± SEM (%)	Figure 4C subsets	Mean ± SEM (%)
Naive	3.45 ± 0.845	DC	5.09 ± 1.83
Treg	19.54 ± 4.55	pDC	1.97 ± 0.57
Effector CD161-	14.86 ± 3.56	Monocytes	3.4 ± 1.15
Effector CD161+	18.77 ± 3.48	NK CD56+ CD16-	1.73 ± 0.61
		NKT CD56+ CD16-	6.66 ± 2.34

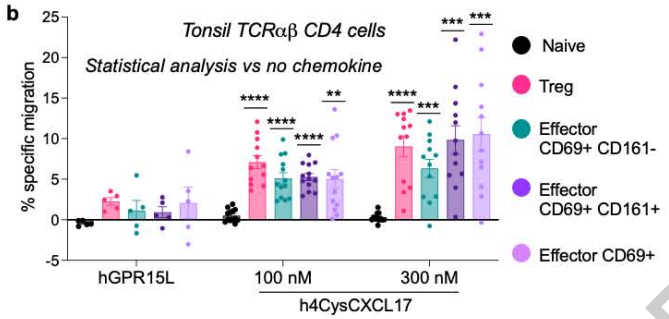

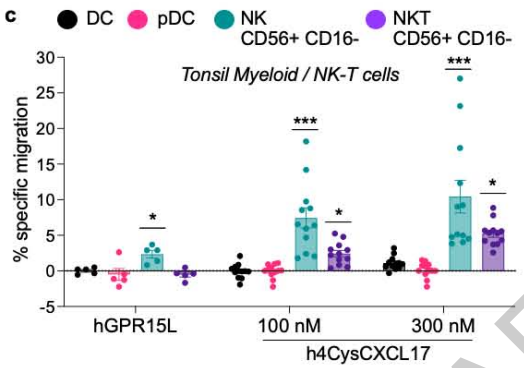

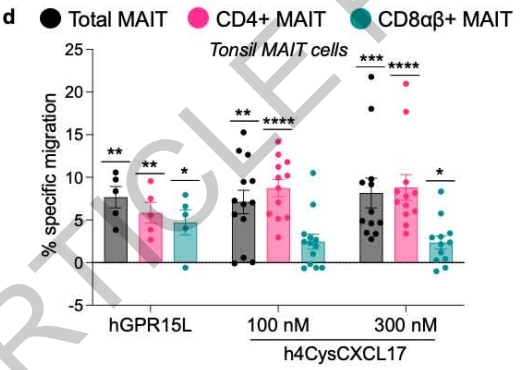

e

Ext. Data 6B subsets	Mean ± SEM (%)	Ext. Data 6C subsets	Mean ± SEM (%)	Ext. Data 6D subsets	Mean ± SEM (%)
Naive	3.18 ± 0.76	DC	4.35 ± 0.97	Total MAIT	16.4 ± 3.17
Treg	7.7 ± 1.15	pDC	2.26 ± 1.09	CD4+ MAIT	17.95 ± 3.4
Effector CD69+ CD161-	11.83 ± 1.4	NK CD56+ CD16-	7.78 ± 2.96	CD8+ MAIT	4.68 ± 1.29
Effector CD69+ CD161+	14.84 ± 1.47	NKT CD56+ CD16-	3.95 ± 0.88		
Effector CD69+	18.05 ± 3.67				

Extended Data Fig. 6

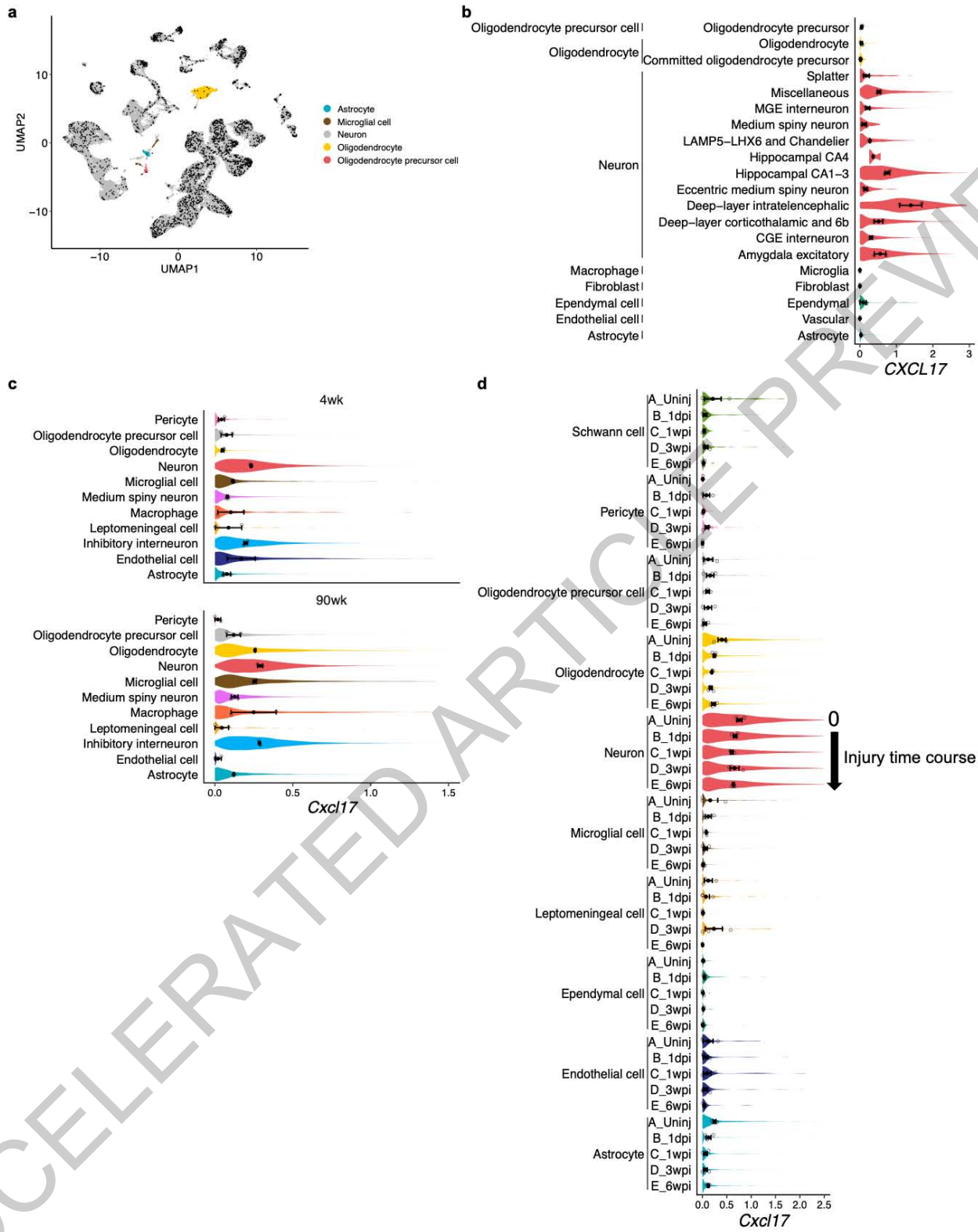

Extended Data Fig. 7

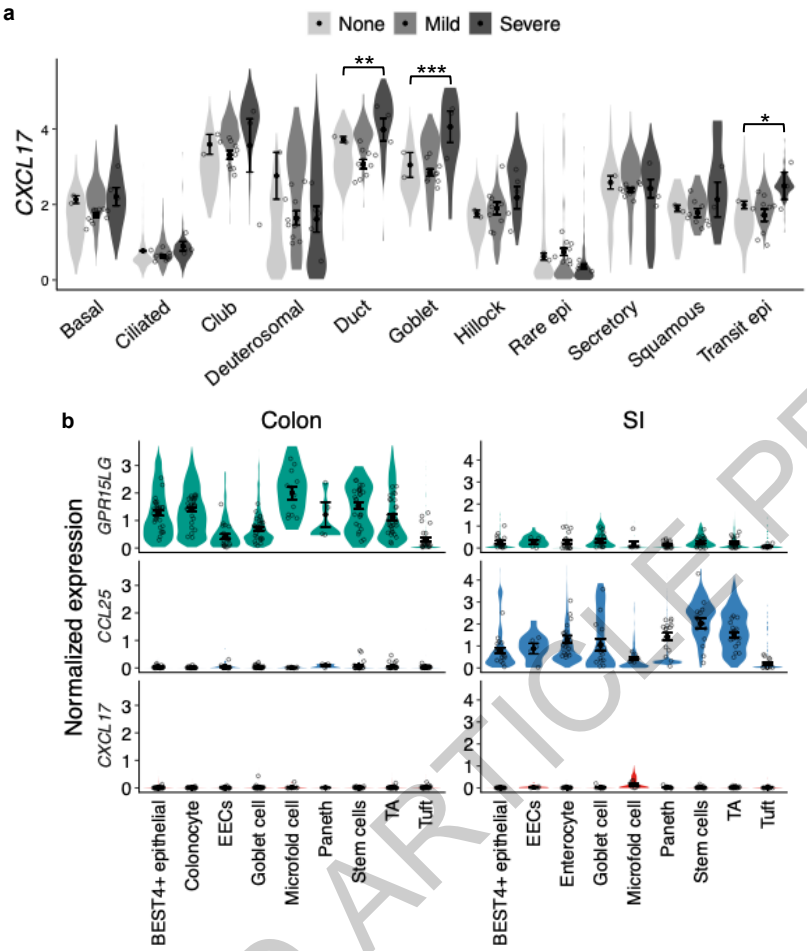

Extended Data Fig. 8

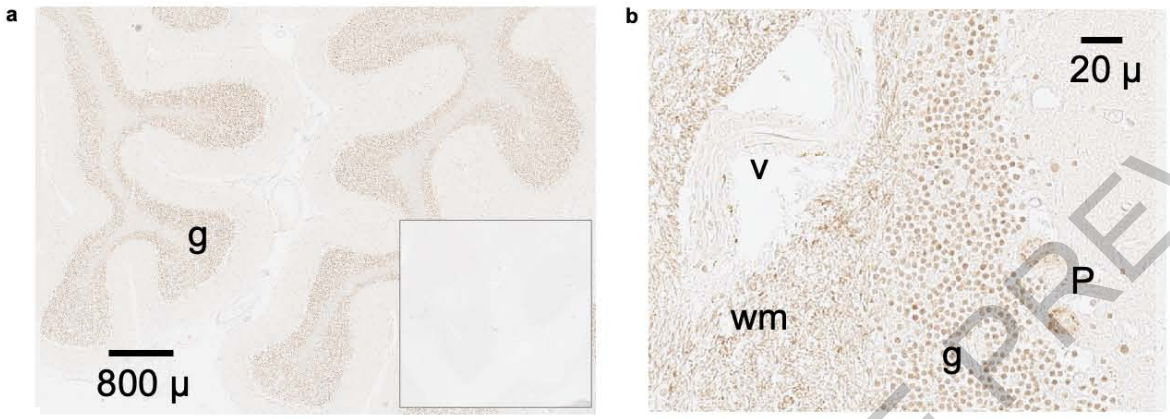

Extended Data Fig. 9

nature portfolio

Corresponding author(s): Borja Ocon, Menglan Xiang, Yuhan Bi

Last updated by author(s): Aug 12, 2024

Reporting Summary

Nature Portfolio wishes to improve the reproducibility of the work that we publish. This form provides structure for consistency and transparency in reporting. For further information on Nature Portfolio policies, see our Editorial Policies and the Editorial Policy Checklist.

Statistics

For all statistical analyses, confirm that the following items are present in the figure legend, table legend, main text, or Methods section.

n/a	Confirmed	
☐	☒	The exact sample size (*n*) for each experimental group/condition, given as a discrete number and unit of measurement
☐	☒	A statement on whether measurements were taken from distinct samples or whether the same sample was measured repeatedly
☐	☒	The statistical test(s) used AND whether they are one- or two-sided *Only common tests should be described solely by name; describe more complex techniques in the Methods section.*
☐	☒	A description of all covariates tested
☐	☒	A description of any assumptions or corrections, such as tests of normality and adjustment for multiple comparisons
☐	☒	A full description of the statistical parameters including central tendency (e.g. means) or other basic estimates (e.g. regression coefficient) AND variation (e.g. standard deviation) or associated estimates of uncertainty (e.g. confidence intervals)
☐	☒	For null hypothesis testing, the test statistic (e.g. *F*, *t*, *r*) with confidence intervals, effect sizes, degrees of freedom and *P* value noted *Give P values as exact values whenever suitable.*
☒	☐	For Bayesian analysis, information on the choice of priors and Markov chain Monte Carlo settings
☒	☐	For hierarchical and complex designs, identification of the appropriate level for tests and full reporting of outcomes
☒	☐	Estimates of effect sizes (e.g. Cohen's *d*, Pearson's *r*), indicating how they were calculated

Our web collection on statistics for biologists contains articles on many of the points above.

Software and code

Policy information about availability of computer code

Data collection	Flow Cytometry: Fortessa analyzer (BD) and Aria III sorter (BD); scRNAseq: captured with 5' chemistry, processed with v2 or v3 kit (10x Genomics) and sequenced on the Illumina NovaSeq X platform; Luciferase assay: the Dual-Gia Luciferase assay system (Promega) and a Turner, TD-20/20 luminometer; RNAscope imaging: a light microscope (Olympus BX53) and attached camera (Olympus DP73); Confocal imaging: Nikon and Zeiss 880 microscope.
Data analysis	Single-cell RNA-seq data analysis: Published 5' 10x Genomics scRNAseq data from the human airway, lung, stomach, pancreas, salivary gland, CSF, cervix, small intestine, colon, skin, blood, thymus, and lymph node were processed to evaluate leukocyte chemoattractant receptor expression. 5' 10X Genomics scRNAseq data from the Human Protein Atlas was analyzed for cell type-specific GPR25 expression, and 3' or 5' 10X data from the human airway, gut, brain and other tissues, and the mouse brain and spinal cord were assessed for CXCL17 expression. For data generated in this study, reads were mapped to the GRCh38 reference genome using Cell Ranger. Hashtag demultiplexing was performed using the HTODemux function of the "Seurat" package. Per cell normalization of raw count data was performed using the NormalizeData function of "Seurat" or the deconvolution method implemented in the computeSumFactors function from the "scran" package. Count data was log transformed using the logNormCounts function from the "scater" package with a pseudo count of 1. The "batchelor" package was used to perform between batch normalization of gene expression using the multiBatchNorm function. When published UMAP coordinates were unavailable, data was integrated using the fastMNN function from the "batchelor" package and UMAPs were computed using the R implementation from the umap package. Gene imputation was performed on log-normalized count data within each batch using the original implementation of the MAGIC (Markov Affinity-based Graph Imputation of Cells) algorithm with optimized parameters (t = 2, k = 9, ka = 3). Imputed data was presented in all figures and for trajectory analysis we used magicBatch (https://github.com/kbrulois/magicBatch) followed by tSpace. GPCR binding site similarity analysis: Pairwise GPCR binding site similarity data was obtained from Supplementary Dataset 1 of Ngo et al. The GPCR-CoINPocket score was used to quantify the similarity between GPCR binding sites based on their contact strength profiles. The pairwise

similarity data was compiled into a matrix format, and the GPCR labels were matched to official HGNC gene symbols, with any outdated symbols manually updated. Briefly, GPCR-CoINPocket performs a sequence alignment for the transmembrane domains of all GPCRs analyzed and using the ligand interaction patterns across all Pocketome entries, the pairwise similarities of GPCR TM domain sequences were calculated and normalized to control for evolutionarily-conserved TM domain regions. The normalized similarity scores were averaged to generate a final binding site similarity score.
Protein analysis for GPR25 ligand search: Isoelectric point (pI) and molecular weight (MW) of human secreted proteins were calculated in R using the "Peptides" package. Proteins with pI > 8 and MW < 25 kD were identified, and amino acid sequences of the human, mouse, rat, rabbit, dog, cow orthologs were obtained from Ensembl BioMart. To evaluate C-terminal conservation of candidate ligands, sequences of the C-terminal 6 amino acids of all proteins were extracted, and the human C-terminal peptide was aligned with that of each of the other 5 species, where ortholog is present, and sequence similarity was calculated by Protein BLAST. The BLAST bit-scores from all pairwise alignments were averaged for each protein. To determine correlation of tissue expression profiles between C-terminally conserved candidate ligands and GPR25, bulk RNA-seq data for human tissues (excluding lymphoid tissues) were obtained from Human Protein Atlas, and Pearson correlation was performed for the cross-tissue gene expression profiles of GPR25 and the candidate ligands with mean BLAST bit-score > 4.
Flow Cytometry Analysis: FlowJo (Vl0.3)
Image Processing: NIS Elements (Nikon), Zeiss Zen, lmaris (version 9), lmageJ (2.0.0 rc49/1. Sld)
Data Analysis: Microsoft Office Excel (2011)
Statistical Analysis: GraphPad Prism (V10) and R

For manuscripts utilizing custom algorithms or software that are central to the research but not yet described in published literature, software must be made available to editors and reviewers. We strongly encourage code deposition in a community repository (e.g. GitHub). See the Nature Portfolio guidelines for submitting code & software for further information.

Data

Policy information about availability of data

All manuscripts must include a data availability statement. This statement should provide the following information, where applicable:

- Accession codes, unique identifiers, or web links for publicly available datasets
- A description of any restrictions on data availability
- For clinical datasets or third party data, please ensure that the statement adheres to our policy

Raw and processed single-cell RNA-seq data generated in this study are available from the NCBI Gene Expression Omnibus repository under the accession number GSE273397. Supplementary Table 1 lists all published external datasets used in this study. Integrated scRNAseq datasets used for the analyses can be accessed at http://med.stanford.edu/butcherlab/data/GPR25.html. Source data are provided with this paper.

Research involving human participants, their data, or biological material

Policy information about studies with human participants or human data. See also policy information about sex, gender (identity/presentation), and sexual orientation and race, ethnicity and racism.

Reporting on sex and gender	In Figure 4B, we have collected data from two donors for human peripheral mononuclear cells (PBMC) (one male and one female). The number of input cells from the male donor was insufficient for analysis, and only results from the female donor are shown in the article. As of the other experiments, PBMC were obtained from healthy donors and surgically removed tonsils were from the Pathology Tissue Bank, Stanford University, Department of Pathology. Some tissues for RNAscope and IHC were collected sterilely from rapid research autopsies by the Research Autopsy Center at Stanford (RACS), consented under Stanford IRB 63818 and autopsy consent. No sex / gender information was provided to us.
Reporting on race, ethnicity, or other socially relevant groupings	Not applicable.
Population characteristics	Meta data for human subjects in all external datasets used in scRNAseq analyses are provide in Supplementary Table 1.
Recruitment	The study was carried out in accordance with the recommendations of the US National Institutes of Health guidelines, with written informed consent from all subjects.
Ethics oversight	The protocol was approved by the Stanford University Institutional Review Board.

Note that full information on the approval of the study protocol must also be provided in the manuscript.

Field-specific reporting

Please select the one below that is the best fit for your research. If you are not sure, read the appropriate sections before making your selection.

☒ Life sciences ☐ Behavioural & social sciences ☐ Ecological, evolutionary & environmental sciences

For a reference copy of the document with all sections, see nature.com/documents/nr-reporting-summary-flat.pdf

Life sciences study design

All studies must disclose on these points even when the disclosure is negative.

Sample size	No method was used to predetermine sample size. A minimum of 3 biological replicates were used for each experiment since it is necessary to achieve statistical significance.
Data exclusions	No data was excluded.
Replication	All attempts at replication were successful.
Randomization	Mice of similar age and sex were used for all the experiments reported. Animals were allocated to groups based on their genotype.
Blinding	For Immunofluorescence studies to quantify T cells: Sections were counted unblinded by two individuals. As validation, a third individual counted representative sections single blinded. For other studies: Researchers were not blinded but were as unbiased as possible when acquiring and analyzing data.

Reporting for specific materials, systems and methods

We require information from authors about some types of materials, experimental systems and methods used in many studies. Here, indicate whether each material, system or method listed is relevant to your study. If you are not sure if a list item applies to your research, read the appropriate section before selecting a response.

Materials & experimental systems

n/a	Involved in the study
☐	☒ Antibodies
☐	☒ Eukaryotic cell lines
☒	☐ Palaeontology and archaeology
☐	☒ Animals and other organisms
☒	☐ Clinical data
☒	☐ Dual use research of concern
☒	☐ Plants

Methods

n/a	Involved in the study
☒	☐ ChIP-seq
☐	☒ Flow cytometry
☒	☐ MRI-based neuroimaging

Antibodies

Antibodies used

Antibodies used are descripted as following: Color species target (clone) company application:
BV421 anti mouse Ki67 (16A8) Biolegend flow cytometry
BV650 anti mouse CD69 (H1-2F3) Biolegend flow cytometry
PercpCy5.5 anti mouse TCR□□ (GL3) Biolegend flow cytometry
AF700, anti mouse NK1-1 (S17016D) Biolegend flow cytometry
APCCy7 anti mouse CD3 (145-2c11) Biolegend flow cytometry
BV421 anti mouse CD8□ (Ly-3) Biolegend flow cytometry
AF647 anti mouse CD90.1-Thy1.1 (OX-7) Biolegend flow cytometry
BV711 anti mouse CD4 (RM4-5) Biolegend flow cytometry
FITC anti mouse CD45.2 (104) BD flow cytometry
BV605 anti mouse IgA (C10-1) BD flow cytometry
BUV395 anti mouse CD45.1 (A20) BD flow cytometry
BV786 anti mouse CD103 (M290) BD flow cytometry
BUV737 anti mouse B220 (RA3-6B2) BD flow cytometry
PercpCy5.5 anti mouse CD11a (M17/4) Tonbo flow cytometry
PECy7 anti mouse TCR□ (H57-597) Tonbo flow cytometry
PercpCy5.5 anti mouse CD45.1 (A20) eBiosciences flow cytometry
AF700 anti mouse CXCR6 (221002) R&D flow cytometry
PE anti human CD161 (HP-3G10) Biolegend flow cytometry
PE-Cy7 anti human CD103 (Ber-ACT8) Biolegend flow cytometry
PercpCy5.5 anti human CD45RA (HI100) Biolegend flow cytometry
AF700 anti human CD69 (FN50) Biolegend flow cytometry
APC-Cy7 anti human CD25 (M-A251) Biolegend flow cytometry
BV421 and PercpCy5.5 anti human CD3□ (UCHT1) Biolegend flow cytometry
BV785 anti human CD4 (RPA-T4) Biolegend flow cytometry
BV650 anti human CD19 (HIB19) Biolegend flow cytometry
APC anti human CD14 (HCD14) Biolegend flow cytometry
BV605 anti human CD45RO (UCHL1) Biolegend flow cytometry
BV650 anti human CD62L (DREG-56) Biolegend flow cytometry
PE anti human CD123 (S18016C) Biolegend flow cytometry
BV421 anti human HLA/DR (L243) Biolegend flow cytometry

BV650 anti human CD11c (Bu15) Biolegend flow cytometry
BUV395 anti human CD8 (2ST8.5H7) BD flow cytometry
BUV737 anti human TCR (T10B91A-31) BD flow cytometry
BV711 anti human TCR V7.2 (OF 5A-12) BD flow cytometry
BUV395 anti human CD56 (NCAM16.2) BD flow cytometry
FITC anti human CD16 (3G8) BD flow cytometry
APC anti human TCR (11F2) Miltenyi flow cytometry
AF488 anti mouse Foxp3 (150D) Biolegend flow cytometry
AF488 anti human Foxp3 (PCH101) eBioscience flow cytometry
Aqua (510) fixable live / dead cell stain Thermoscientific
N/A anti mouse CD28 (37.51) eBiosciences T cell activation
N/A anti mouse CD3 (145-2c11) eBiosciences T cell activation
PE anti mouse CD45 (30-F11) Biolegend flow cytometry
FITC anti human CD45RA (HI100) Biolegend flow cytometry
PercpCy5.5 anti human HLA (L243) BD flow cytometry
BUV737 anti human TCR (IP26) BD flow cytometry
BUV395 anti human IgD (IA6-2) BD flow cytometry
PECy7 anti human CD69 (FN50) Biolegend flow cytometry
BV605 anti human CD45RO (UCHL1) Biolegend flow cytometry
BV421 anti human CD8 (SK1) Biolegend flow cytometry
BV786 anti human CD4 (SK3) Biolegend flow cytometry
APCCy7 anti human CD38 (HIT2) Biolegend flow cytometry
AF700 anti human CD19 (HIB19) Biolegend flow cytometry
DeLight633 anti-CD31 (clone 390) InvivoMab Immunofluorescence
APC anti mouse TCR (clone H57-597) Biolegend Immunofluorescence
PE anti mouse CD103 (clone 2E7) Biolegend Immunofluorescence
N/A anti mouse CD8 (clone 4SM15) Invitrogen Immunofluorescence
N/A anti mouse CD4 (clone RM4-5) Biolegend Immunofluorescence
AF488 secondary antibody Invitrogen Immunofluorescence

Validation

Antibodies used came from commercial vendors. We have thoroughly selected all our commercially available antibodies from commercial sources based on the validation provided by the manufacturer for the indicated species (i.e. mouse or human) and for the application(s) they sell the antibody for (i.e. Flow cytometry or Immunofluorescence in our studies). Any information regarding the validation performed by the manufacturer can be retrieved on the manufacturers' websites using the information that we provided in the "Antibodies used" section above.
For each antibody, the staining strategy was thoroughly optimized in the lab prior to its use in this study. We started with the dilution recommended by the manufacturer or publication and then further optimized each dilution using appropriate isotype controls and single stains.

Eukaryotic cell lines

Policy information about cell lines and Sex and Gender in Research

Cell line source(s)	Platinum-E (Plat-E) Retroviral Packaging Cell Line was purchased from Cellbiolabs. L1-2 cell line (pre-B cell mouse lymphoma) was lab stock.
Authentication	Platinum-E (Plat-E) Retroviral Packaging Cell Line was authenticated by Cellbiolabs. Example of citation: PMID (37597518) L1-2 cell line was authenticated by Eugene Butcher lab. Example of citation: PMID (22696441)
Mycoplasma contamination	Platinum-E cells were tested mycoplasma negative by Cellbiolabs. L1-2 cells were tested mycoplasma negative in lab.
Commonly misidentified lines (See ICLAC register)	No commonly misidentified cell lines were used in the study.

Animals and other research organisms

Policy information about studies involving animals; ARRIVE guidelines recommended for reporting animal research, and Sex and Gender in Research

Laboratory animals	All mice in this study were maintained in specific pathogen-free (SPF) facilities at the Veterans Affairs Palo Alto Health Care System (VAPAHCS). B6/SJL Prprc Pep3BoyJ (CD45.1), C57B6/J CD45.2 and Rag1-/- mice were purchased from Jackson laboratories. The Cxcl17-/- mouse strain (C57BL/6NAtm1Brd Cxcl17tm1b(EUCOMM)Wtsi/MbpMmucd) RRID:MMRRC_047263-UCD, was obtained from the Mutant Mouse Resource and Research Center (MMRRC) at University of California at Davis, an NIH-funded strain repository, and was donated to the MMRRC by The KOMP Repository, University of California, Davis. Originating from Kent Lloyd, UC Davis Mouse Biology Program mice were purchased from the MMRRC at UC Davis. C57B6/N controls were purchased from the MMRRC as well.
Wild animals	No wild animals were used in the study.
Reporting on sex	Both sexes were included in experiments, except for homing experiments where the female GU tract was required.
Field-collected samples	No field-collected samples were used in the study.

Ethics oversight	Animals were maintained in accordance to US National Institutes of Health guidelines, and experiments were approved by Stanford University Institutional Animal Care and Use Committee.

Note that full information on the approval of the study protocol must also be provided in the manuscript.

Plants

Seed stocks	*Report on the source of all seed stocks or other plant material used. If applicable, state the seed stock centre and catalogue number. If plant specimens were collected from the field, describe the collection location, date and sampling procedures.*
Novel plant genotypes	*Describe the methods by which all novel plant genotypes were produced. This includes those generated by transgenic approaches, gene editing, chemical/radiation-based mutagenesis and hybridization. For transgenic lines, describe the transformation method, the number of independent lines analyzed and the generation upon which experiments were performed. For gene-edited lines, describe the editor used, the endogenous sequence targeted for editing, the targeting guide RNA sequence (if applicable) and how the editor was applied.*
Authentication	*Describe any authentication procedures for each seed stock used or novel genotype generated. Describe any experiments used to assess the effect of a mutation and, where applicable, how potential secondary effects (e.g. second site T-DNA insertions, mosiacism, off-target gene editing) were examined.*

Flow Cytometry

Plots

Confirm that:

☒ The axis labels state the marker and fluorochrome used (e.g. CD4-FITC).

☒ The axis scales are clearly visible. Include numbers along axes only for bottom left plot of group (a 'group' is an analysis of identical markers).

☒ All plots are contour plots with outliers or pseudocolor plots.

☐ A numerical value for number of cells or percentage (with statistics) is provided.

Methodology

Sample preparation	All sample preparation protocols are thoroughly outlined in the corresponding section of Material and Method.
Instrument	Fortessa analyzer (BD) and Aria lll sorter (BD)
Software	Data collection: BDFACSDiva. Data analysis: FlowJo (Vl0.3)
Cell population abundance	For homing experiments, cell purity and percentage of transduction (% Thy1-1+ cells) were assessed by flow cytometry right before adoptive cell transfer into recipients. These numbers were used to normalize our homing results by transduction efficiency in the input population.
Gating strategy	Cell populations of interest were identified by cell size in a FSC-A vs. SSC-A plot. Single cells were discriminated in an FSC-H vs. FSC-W plot followed by SSC-H vs. FSC-W plot. Aqua BV510 was used to separate dead/dying cells from healthy cells. Within singlets and live cells as a starting point, we followed different gating strategies depending on the experiment and cell subset of interest. All these strategies, whether for analysis or cell sorting, are outlined in detail in Supplementary Figure 1A-D.

☒ Tick this box to confirm that a figure exemplifying the gating strategy is provided in the Supplementary Information.